Design Strategies for Ultra-high Efficiency Photovoltaics

Thesis by
Emily Cathryn Warmann

In Partial Fulfillment of the Requirements
for the Degree of
Doctor of Philosophy

California Institute of Technology
Pasadena, California

2014

(Defended May 9, 2014)

Acknowledgements

The people I have worked and interacted with during my time here have been absolutely essential to the work described in this thesis and have been an integral part of my education and development as a scientist. The material and intellectual contributions of those I have worked with are so numerous it would be impossible to list them all here, but there are some I must thank in particular.

I must begin by thanking my advisor, Professor Harry Atwater. He has provided guidance, encouragement, insight and inspiration throughout my studies. He has also been a model of optimism and curiosity that I hope to emulate.

I also thank the other members of my candidacy and thesis committees: Professors Kaushik Bhattacharya, Julia Greer, and Austin Minnich, for their guidance and feedback on my work.

I am especially grateful to Professor Bhattacharya and Professor Guruswami Ravichandran for being kind enough to let me join in their group meetings for a time and stay in touch with my mechanical engineering roots.

Much of my work has been part of various team efforts. I would not have been able to accomplish what I did on my own, and so I must thank my collaborators on my various projects. Prof. Koray Aydin, Dennis Callahan, Prof. Marina Leite and Erika Garcia were all vital to my work on novel epitaxial templates. I learned so much from all of them. My last two years have been immeasurably enriched by being a part of the Full Spectrum Team. Many, many thanks to Carissa Eisler, Emily Kosten, Cris Flowers, John LLoyd, Sunita Darbe, Kelsey Whitesell, Prof. Matt Escarra and Michelle Dee. Go Rainbow Warriors!

I am fortunate to have had the opportunity to work with the members of the Atwater group. To interact on a daily basis with an interdisciplinary group of such brilliant individuals has been an amazing experience. Those I am particularly thankful to include Melissa Archer, Anna Beck, Jeff Bosco, Ryan Briggs, Ana Brown, Stanley Burgos, Chris Chen, Carrie Hofmann, Min Jang, Seokmin Jeon, Greg Kimball, Lise Lahourcade, Prof. Jiun-Haw Lee, Andrew Leenheer, Gerald Miller, Prof. Deirdre O'Carroll, Ragip Pala, Imogen Pryce, Elizabeth Santori, Matthew Shaner,

Matt Sheldon, Amanda Shing, Pierpaolo Spinelli, Josh Spurgeon, Prof. Nick Strandwitz, Luke Sweatlock, Faisal Tajdar, Victor Brar, and Samantha Wilson.

I am particularly thankful for the officemates I have had while at Caltech. Dan Turner-Evans, Carissa Eisler, Gerald Miller, Ana Brown, and Krista Langeland, thank you for putting up with my tendency to talk to myself. I am grateful for all the conversations about data, what's going wrong and what's going right.

In the Atwater group, April Neidholdt, Lyra Haas, Jennifer Blankenship, and Tiffany Kimoto, have enriched my experience, not only by making sure everything runs smoothly and organizing our group retreats and events, but also for helping to make the Atwater group a friendly and enjoyable place to work. I would also like to thank the Mechanical Engineering administrative staff, particularly Cheryl Geer, for smoothing out the inevitable paperwork and keeping us all from slipping through the cracks.

Finally, I would like to thank my family and friends for all the love and support that has kept me going during the highs and lows. Especially Darrel Jenerette, who reminds me that this is fun and interesting.

Abstract

While concentrator photovoltaic cells have shown significant improvements in efficiency in the past ten years, once these cells are integrated into concentrating optics, connected to a power conditioning system and deployed in the field, the over all module efficiency drops to only 34 to 36%. This efficiency is impressive compared to conventional flat plate modules, but it is far short of the theoretical limits for solar energy conversion. Designing a system capable of achieving ultra-high efficiency of 50% or greater cannot be achieved by refinement and iteration of current design approaches.

This thesis takes a systems approach to designing a photovoltaic system capable of 50% efficient performance using conventional diode-based solar cells. The effort began with an exploration of the limiting efficiency of spectrum splitting ensembles with 2 to 20 sub-cells in different electrical configurations. Incorporating realistic non-ideal performance with the computationally simple detailed balance approach resulted in practical limits that are useful to identify specific cell performance requirements. This effort quantified the relative benefit of additional cells and concentration for system efficiency, which will help in designing practical optical systems.

Efforts to improve the quality of the solar cells themselves focused on the development of tunable lattice constant epitaxial templates. Initially intended to enable lattice-matched multijunction solar cells, these templates would enable increased flexibility in band gap selection for spectrum splitting ensembles and enhanced radiative quality relative to metamorphic growth. The III-V material family is commonly used for multijunction solar cells both for its high radiative quality and for the ease of integrating multiple band gaps into one monolithic growth. The band gap flexibility is limited by the lattice constant of available growth templates. The virtual substrate consists of a thin III-V film with the desired lattice constant. The film is grown strained on an available wafer substrate, but the thickness is below the dislocation nucleation threshhold. By removing the film from the growth substrate, allowing the strain to relax elastically, and bonding it to a supportive handle, a template with the desired lattice constant is formed. Experimental efforts towards this structure and

initial proof of concept are presented.

Cells with high radiative quality present the opportunity to recover a large amount of their radiative losses if they are incorporated in an ensemble that couples emission from one cell to another. This effect is well-known, but has been explored previously in the context of sub-cells that independently operate at their maximum power point. This analysis explicitly accounts for the system interaction and identifies ways to enhance over-all performance by operating some cells in an ensemble at voltages that reduce the power converted in the individual cell. Series-connected multijunctions, which by their nature fascilitate strong optical coupling between sub-cells, are re-optimized with substantial performance benefit.

Photovoltaic efficiency is usually measured relative to a standard incident spectrum to allow comparison between systems. Deployed in the field systems may differ in energy production due to sensitivity to changes in the spectrum. The series-connection constraint in particular causes system efficiency to decrease as the indicent spectrum deviates from the standard spectral composition. This thesis performs a case study comparing performance of systems over a year at a particular location to identify the energy production penalty caused by series-connection relative to independent electrical connection.

Contents

List of Figures

List of Tables

Chapter 1

Introduction

1.1 Solar energy: potential, progress and room for improvement

Photovoltaics, which convert light from the sun into electrical energy, are a growing part of the world's energy production portfolio. The sun delivers 1.6×10^5 TW [1]. Current combined power consumption across the globe is approximately 17 Tw [2], which indicates that harnessing a small fraction of the sun's power would be sufficient to meet all of present and projected energy needs without requiring any additional fuel. The prospect of harnessing the sun for cheap, clean energy has made photovoltaics one of the most prominent renewable energy technologies under development today. Presently less than 1.5% of the world's energy is produced by photovoltaics [2]. While this is a small number, it has grown on average 57% annually over the past 6 years [3]. In 2013, 20% of the new electricity generation capacity added in the United States was solar power [4].

In order to be adopted at a very large scale and produce a large percentage of the world's electricity, photovoltaics must be able to produce power at a cost comparable to or lower than conventional energy generation technologies. A useful figure of merit that allows comparisons between different energy production technologies is the Levelized Cost of Energy or LCOE [5]. At its simplest, this calculation divides the total costs of a power plant, both initial capital and ongoing fuel consumption, by the total energy production expected from a power plant. The cost of ongoing fuel requirements and value of the ongoing energy production are both reduced to

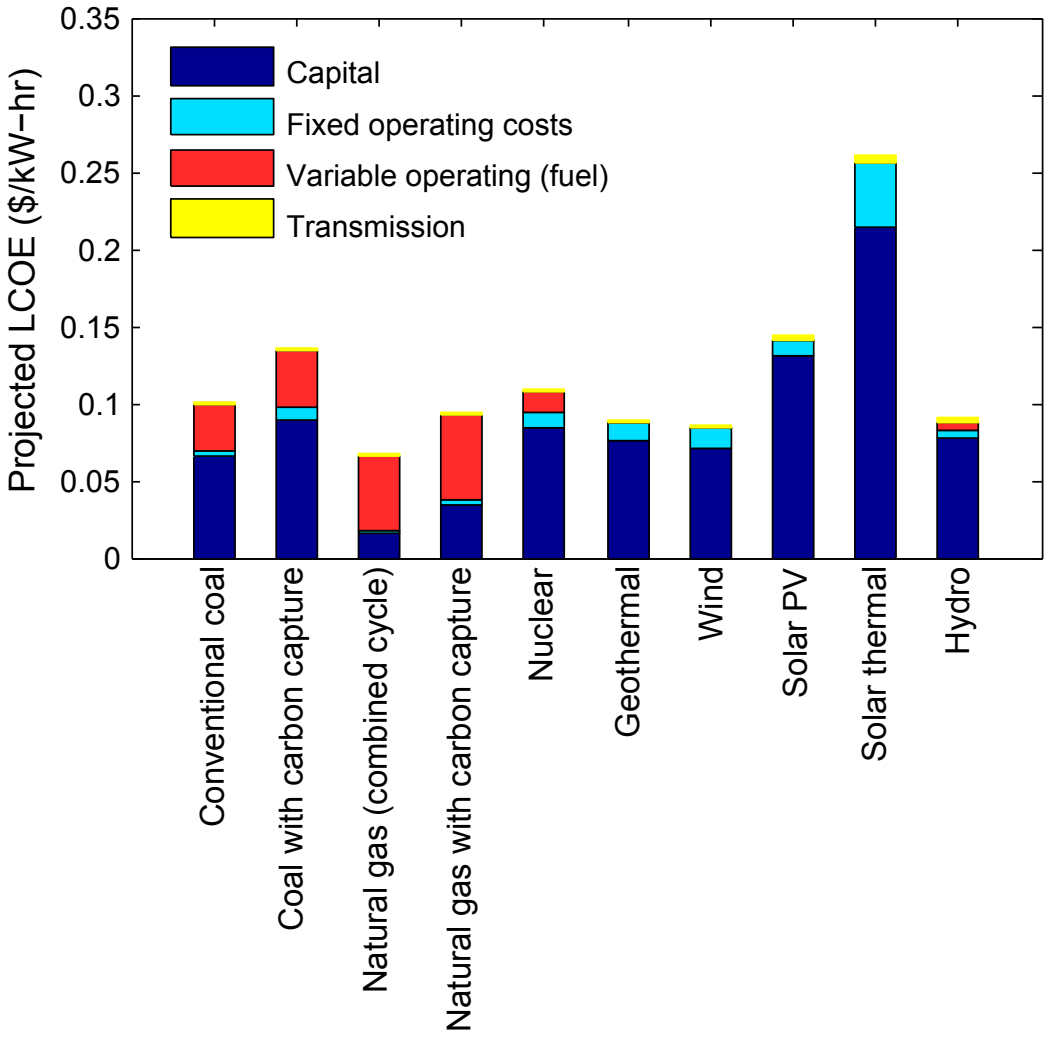

Figure 1.1. Projected LCOE for various electricity generation technologies in 2018.

a net present value by discounting the value of future transactions. Figure 1.1 shows the DOE projection of the 2018 LCOE for a variety of different generation technologies relative to coal-fired power, with the capital and ongoing components separated cite. The LCOE for fossil fuel-based energy sources such as coal or gas plants is largely driven by the cost of the fuel source required per unit of energy produced [3]. By contrast, for solar installations, this cost is primarily determined by the cost of installing the plant initially, the discount rate, and the amount of energy the installation produces over the course of its service life.

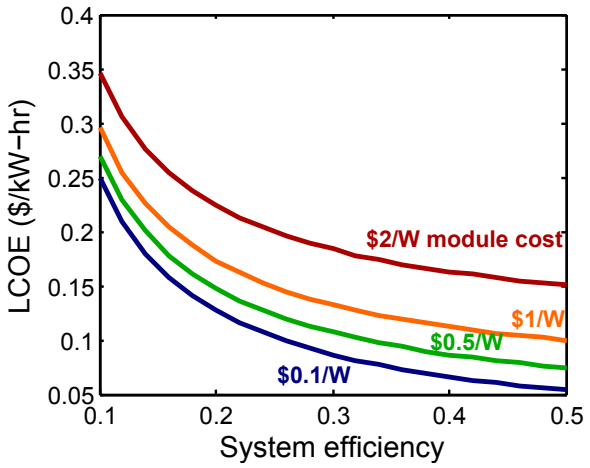

Figure 1.2. The LCOE of a fixed area installation with $3 per m2 fixed costs and different $/W module cost scenarios. The fixed costs independent of generating capacity, such as permitting and land acquisition, create a strong benefit to increased efficiency at any module cost level.

1.2 Efficiency improvements can be a way to reduce energy costs

Given that the cost of solar energy is determined when the system is installed, there are essentially only two ways to reduce the LCOE of photovoltaics. Either the cost of installing a system must be reduced or the amount of energy the system produces for a given installation cost must be increased. Consider a hypothetical photovoltaic installation. At present prices, that facility will cost $4 to $6/W to install [5], with about half of that cost taken by the photovoltaic modules themselves. The price of the modules themselves is typically reported relative to their rated generating capacity under standard test conditions in $/Wp. Two different modules with different efficiency but the same $/Wp (and the same relative performance over the course of a year, a good first order assumption for similar technologies) will have the same LCOE, all other things being equal. Figure 1.2 shows the LCOE of this hypothetical installation as a function of efficiency for different module $/Wp values, assuming a discount rate of 8% and a fixed cost per area of $3/m^2.

Decreasing the cost of a photovoltaic installation can be done through improvements in the manufacturing process, reduction of materials consumption, design improvements that reduce the cost of mounting hardware and installation labor or simplification of the permitting and approval process. These are all active areas of research in both industrial, government and academic settings. There are also many efforts to increase the efficiency of photovoltaic systems, such as by improving the design of specific cell types, improving material quality, improving manufacturing consistency or control, and other means. Most of these efforts are likely to produce only small (but not unmeaningful) improvements in efficiency. This thesis instead explores design changes that can achieve ultra-high efficiency.

1.3 Efficiency limits for photovoltaics

There are several possible limits to the efficiency of solar energy conversion. The Carnot limit for an ideal process operating between the temperature of the sun (5600 K) and the temperature of the earth (300K) is 95% [6]. This limit assumes a purely one-way transfer of energy from the sun to the earth and a reversible process converting that energy to work. For solar cells, the limit is reduced to 92%, because the specific energy transfer process is radiation [7]. Because radiation is a reciprocal process, any object receiving radiant energy from the sun will also return some radiation to the sun. In a closed system this reciprocal radiation would not change the efficiency limit, but the solar system cannot be considered closed. Thus 93.3% efficiency, sometimes termed the Landsberg limit, is the maximum possible efficiency for a solar cell at 300 K, assuming no entropy generation.

1.3.1 Conventional photovoltaic operation

Solar cells are typically made of semiconductor materials that have a particular type of electronic structure. These materials have completely filled valence bands and completely empty conduction bands at absolute zero. The valence and conduction bands are separated in energy by a value Eg, the band gap value. When a semiconductor

absorbs light, some of the electrons in the semiconductor are promoted into that material's mostly empty valence band. The excited electrons leave empty states, termed "holes", behind in the valence band. In an isolated chunk of semiconductor with no additional electronic structure, the excited conduction band electrons will fall back to the valence band holes, termed "recombine", and the material will return to its original state. The electron-hole recombination may be radiative, in which case it will result in the emission of a photon with the same energy as the band gap, Eg, or it may come through interaction with some defect in the material, which will disipate the excess electron energy through a combination of lattice vibrations and lower energy photon emission. Defect-mediated recombination is termed "nonradiative", because it results in no photons that can be re-absorbed by the material. In an ideal material, all recombination will be radiative [8].

Under steady illumination with a constant flux of photons onto the semiconductor, the absorbed photons will result in a population of excited electron-hole pairs with a chemical potential, as described by Wurfel [9]. The rate of electron-hole recombination is proportional to the chemical potential. Consequently, under illumination the population of excited electron-hole pairs will accumulate until the recombination and absorption rates are equal.

In a solar cell, an internal diode separates the excited electron-hole pairs and allows current to be extracted from the device. At short circuit in an ideal cell, the extracted current is equal to the absorbed photon flux and no carriers are lost to recombination. However, no power is extracted at short circuit, because the voltage across the device is zero [8]. The diode allows current to be extracted at higher voltages, but the voltage is equal to the chemical potential of the excited carrier populations, meaning that some radiative recombination is inevitable. Figure 1.3 shows the J-V relationship for an ideal solar cell that results from the recombination rate relationship. At open circuit, the recombination rate is equal to the photon absorption rate and no current is collected.

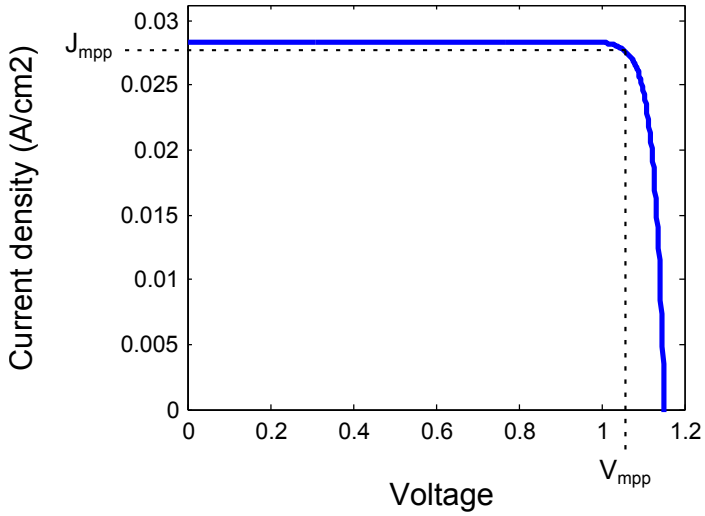

Figure 1.3. J-V relation for an ideal solar cell of 1.4 eV band gap. The voltage and current density of the maximum power operating point (mpp) are indicated.

1.3.2 Efficiency limits specific to conventional photovoltaics

The thermodynamic limits discussed in the section 1.3 make no assumptions as to the mechanism of energy conversion. If the heat engine is a photovoltaic cell, a variety of other limits combine to reduce the achievable conversion efficiency. A typical single junction solar cell will efficiently convert photons that have energy equal to or slightly greater than the energy band gap value of the material, Eg. Photons with energy less than Eg are not absorbed by the semiconductor, and are simply transmitted through the material. Any photon energy in excess of Eg is transferred to the material's crystal lattice vibrations through thermalization [8]. The energy radiated from the sun closely resembles the spectrum of a black body at 5600 K. As such, that energy is distributed over a wide range of photon energies. Choosing the band gap value of the solar cell to maximize conversion efficiency is then a matter of optimizing the trade-off between photons lost to transmission and photon energy lost to thermalization. Shockley and Queisser used the detailed balance approach to determine that the optimal band gap value for a solar cell receiving light from a 6000 K black body and operating at 300 K is 1.1 eV and the limiting efficiency for this device is 30% [10]. The light incident on a solar cell at the earth's surface has passed through the atmosphere and will have a

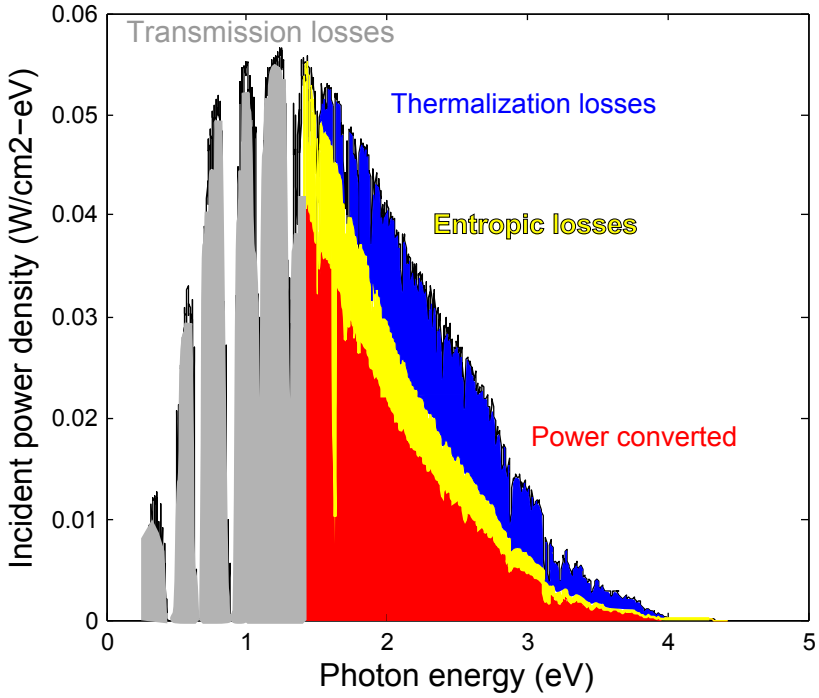

Figure 1.4. Reference spectra representing indicent light from the sun with the power converted by a 1.4 eV single junction solar cell indicated. Losses due to transmission and thermalization are also indicated. Additional losses are due to entropy generation.

different spectral composition due to absorption and scattering by various gases and suspended particles. Repeating this calculation for a solar cell operating at 300 K and receiving a standard spectrum, AM1.5G, that is more representative of the light that penetrates the atmosphere to reach the earths surface identifies a new optimum band gap of 1.34 eV at 33.7% efficiency [11]. Figure 1.4 shows the performance of an ideal solar cell with 1.4 eV band gap relative to the standard AM1.5G spectrum, with the converted power, transmission losses and thermalization losses shaded separately.

1.3.3 Multijunction solar cells

Breaking the solar spectrum into various sub-bands and directing them to different sub-cells that have band gap values better matched to the range of photon energies incident upon them is a well-known way to reduce both thermalization and transmission losses. The current world record for efficiency belongs to a multijunction solar

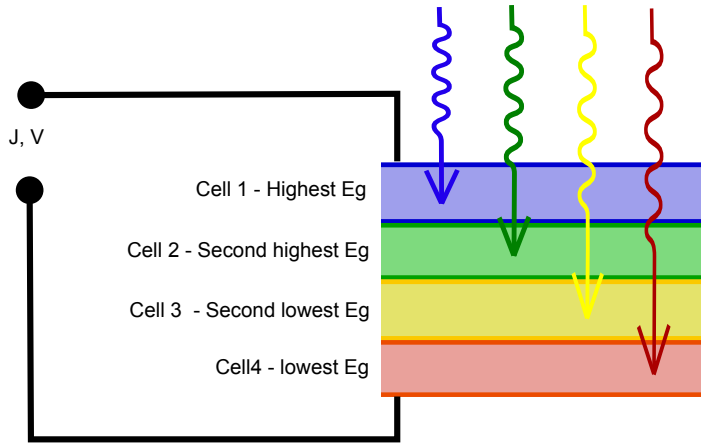

Figure 1.5. Schematic showing the operating principle of multijunction solar cells (MJSCs). Sub-cells are monolithically stacked and connected in electrical series. The spectrum is split amongst the sub-cells by sequential absorption.

cell (MJSC) with four sub-cells [12]. Most commonly, the broadband solar spectrum is divided among the sub-cells by means of sequential absorption. The sub-cells are stacked such that the highest band gap material is on top, where it receives all incident light. The highest band gap sub-cell will absorb the highest energy photons and transmit all other light to the sub-cells below [11]. The various sub-bands of the incident spectrum will be sequentially absorbed by the sub-cells with decreasing band gap values, until the last sub-cell absorbs its share and the remaining low energy photons are lost to transmission. This process is shown schematically in Figure 1.5. At the limit of an infinite stack of sub-cells with infinitessimally different band gaps, the limiting efficiency of this concept is 87% [13].

Practical devices will necessarily have a finite number of sub-cells, and yet they might include many more than the four in the current record device. The benefit of adding additional cells has not yet been explored systematically. Most work in this field has concentrated on extending existing material systems, and the prospective designs are constrained in the number and range of band gaps that can be considered [14]. Practical devices also exhibit loss mechanisms in addition to the radiative emission considered by the classical detailed balance calculation, and they may be integrated into optical and electrical systems that add further losses. Chapter 2 of

this thesis develops modifications to the detailed balance calculation that account for non-ideal behavior and applies this modified calculation to surveying the design space of MJSCs that can achieve ultra high efficiency, even once integrated into a full system with optical and electrical losses.

1.3.4 Alternatives to conventional photovoltaics

The efficiency limits detailed in the sections above assume the photovoltaic system is an ensemble of conventional solar cells. As such, the limits are defined by the absorption and radiative characteristics specific to this type of device. There are concepts for other types of photovoltaic devices, often termed "Third Generation" photovoltaics, that are not necessarily subject to these limits [6]. Cells capable of multiple exciton generation could in principle employ a low band gap material and still minimize thermalization losses by exciting many electrons with each high-energy photon absorbed [15]. Devices that prevent or delay interaction of excited electrons and phonons and allow extraction of only electrons with a specific energy, so-called "hot carrier" solar cells, could in theory operate at the Landsberg limit [16]. While these concepts are theoretically capable of ultra-high efficiency under ideal or near ideal circumstances, as yet no experimental demonstration has achieved efficiency approaching that of conventional photovoltaics. In addition, once realistic non-ideal material behavior is accounted for, the likely performance of these concepts drops to much less impressive levels. For these reasons, this thesis considers only concepts that employ conventional photovoltaic cells in search of ensemble designs capable of ultra-high efficiency.

1.4 Recovering radiative losses

As mentioned in section 1.3.1, all solar cells emit light when operating at a positive voltage. In a single junction cell, this radiative emission is an inevitable loss mechanism that can be minimized by careful engineering of the optical environment of the cell, but never eliminated. In multijunction solar cells, some portion of this radiative

emission may be recovered by directing it to be absorbed in subsequent sub-cells of the ensemble [17]. This process happens naturally in monolithically integrated cells, due to the close index of refraction match between sub-cells [18]. Recent experimental results have documented this phenomenon [19]. Recovering these radiative losses in distributed ensembles of cells can be more challenging due to the need for an additional optical element to engineer the desired photon transmission between sub-cells. If the challenges can be met, the benefits of radiative coupling can be substantial: up to 1% improvement in absolute efficiency, depending on the number of sub-cells in the ensemble [20].

Historically, examinations of the benefit of radiative coupling have assumed that each sub-cell in the ensemble will operate at its individual maximum power point. However, the sub-cell max power point is the voltage and current at which the power benefit of any additional voltage is offset by the loss in power due to increased radiative losses. In a system with radiative coupling, some fraction of the radiated loss is recovered in a different sub-cell. As a consequence, the coupling must be taken into account when calculating the maximum power point of the ensemble as a whole. Chapter 4 of this thesis explores the additional benefit of taking radiative coupling into account when designing an ensemble and determining its maximum power point.

1.5 Designing for energy production

While the efficiency of a photovoltaic system is fairly straightforward to measure and is a convenient metric for comparing different systems, it is not directly used to calculate the LCOE of a system. Instead, the amount of energy the system will generate over its life is used. In cases where the efficiency of a system is fairly constant regardless of the illumination conditions, it can be fair to extrapolate energy production directly from the average irradiance at a particular location over the course of a year. However, not all photovoltaic systems are equally robust under varying spectral conditions [21].

The standard test conditions for measuring photovoltaic system efficiency specify the cell temperature (25C), the illumination level and the spectrum of illumination

[22, 23]. There are a variety of standard spectra intended to represent some average terrestrial or extraterrestrial illumination. In space all spectral variation is due to fluctuations in the sun, and the overall level of variation is small [24]. At any moment, the spectrum at the top of the earth's atmosphere will closely resemble the AM0 (for zero air mass) standard spectrum. To reach the earth's surface, that spectrum must transmit through the atmosphere with a path length that depends on the location, elevation, and time of day and year. The path length is typically reported as the "air mass", or AM, where an air mass of 1 corresponds to the atmospheric depth. The spectrum is attenuated due to molecular and particulate absorption and scattering, and the amount of attenuation is generally proportional to the air mass. As an additional complication, the amount of attenuation is sensitive to the particular composition of the atmosphere along the light path [25]. The atmosphere is not well mixed, and there can be substantial variation in the amount of $C0_2$, ozone, water vapor and particulate matter in the air column in the region of a photovoltaic device. The standard terrestrial reference spectra, AM1.5G and AM1.5D, that are most commonly used for photovoltaic efficiency measurements specify an air mass of 1.5 and a spectral composition that corresponds to a particular set of atmospheric conditions cite [26]. While these conditions in some sense constitute an average of the mid-latitude, mid-day, mid-year environment, at any point in time the actual incident spectrum will have substantial deviation from these references. Because photovoltaics are compared by efficiency measured under these reference spectra, photovoltaic design is shaped by the specific details of these spectra. Spectrum splitting ensembles are optimized for maximum efficiency converting AM1.5D or G. Systems with series-connected cells are designed such that each sub-cell is designated an equal number of photons under the reference spectrum. When the actual incident spectrum deviates from the reference, the system may perform better or worse [21]. Chapter 5 of this thesis explores the impact of the projected spectral variation over the course of a year on spectral splitting ensembles with different numbers of sub-cells and different types of electrical configurations.

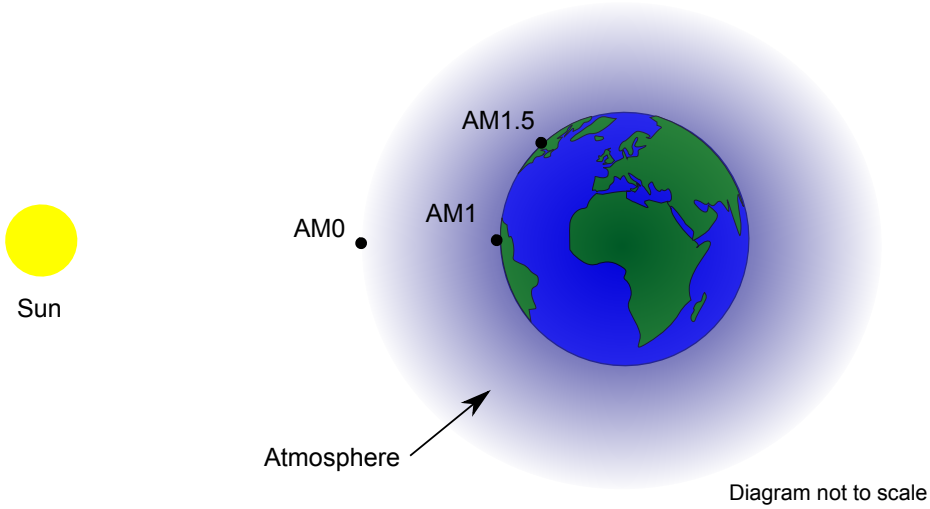

Figure 1.6. Schematic of air mass, unit of measurement for atmospheric transmission length. AM0 corresponds to a point at the top of the atmosphere, and AM1 to the atmospheric depth normal to the earth's surface at sea level. Other air mass values are path lengths relative to the value of AM1.

1.6 New substrates for monolithic MJSCs

While ultra-high efficiency is a valuable goal for reducing LCOE, improving the efficiency and reducing cost of conventional MJSCs also has the potential to reduce energy costs. The monolithic MJSC consists of sub-cells that are grown one on top of another in a series of chemical vapor deposition steps on the same substrate. Ensuring high material quality requires either that the materials all have the same crystal lattice constant as the substrate material or that some intermediate layer be able to provide a transition in lattice constant while introducing a minimum of lattice defects. Currently high-efficiency MJSCs are made from different alloys in the III-V family of materials [14, 27]. As figure 1.7 shows, these materials span a large range of band gap values and lattice constants. However, focusing on the InAlGaAsP subset of materials, there is a very limited range of lattice constants that offer a substantial range of lattice-matched band gap values. Unfortunately, the lattice constants that do offer a desirable range of band gaps do not correspond to lattice constant of the commercially available substrates, which are GaAs and InP. At the lattice constant

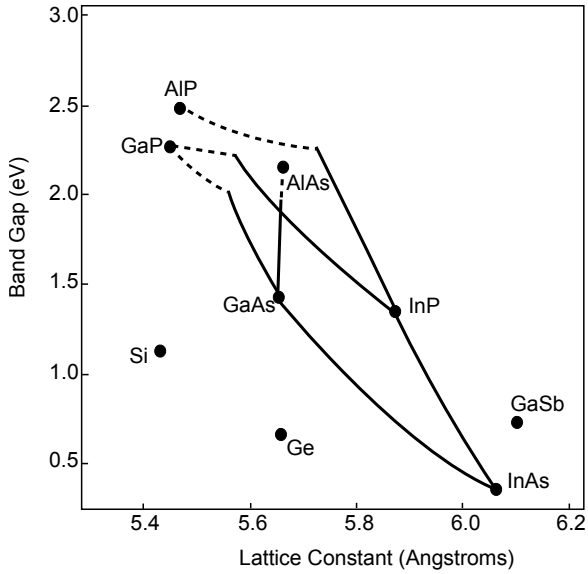

Figure 1.7. Band gap versus lattice constant for a subset of the III-V material family. Dots represent binary compounds, curves represent ternary alloys of their binary endpoints, and the space enclosed by curves consists of quaternary alloys. Elemental semiconductors silicon and germanium added for reference.

of InP, the highest available band gap value is 1.55 eV, which is too low for high efficiency two or three junction MJSCs. Conversely, the minimum band gap available at the GaAs lattice constant is 1.42 eV, which is far too high. Extending the system to include germanium, shown on figure 1.7, still results in the middle junction band gap being constrained to be too high.

The conventional approach to circumvent the problem of the substrate lattice constant constraining band gap selection is to use compositionally graded buffer layers to transition the substrate lattice constant to a different value [28]. The buffer layer growth is optimized to provide the maximum amount of strain relief in the material per individual dislocation, but it inevitably results in at least 10^5 dislocations per cm^2 to be introduced. These electrically active dislocations propagate upward into the solar cells grown on top of them and will tend to increase the amount of non-radiative recombination in the cells. Another approach expands the available material family to include InGaAsSbN, which can be grown lattice-matched to GaAs at a band

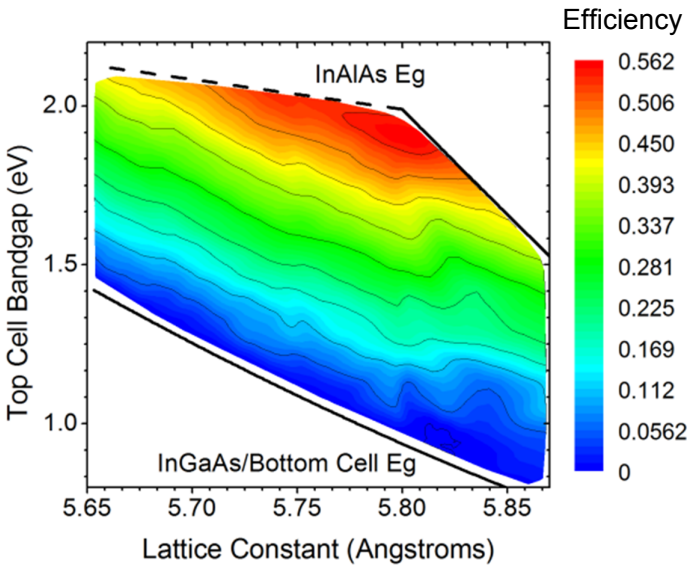

Figure 1.8. Map of detailed balance efficiency of lattice-matched triple junction cells vs lattice constant and top cell band gap. The bottom cell is InGaAs with the specific composition determined by the lattice constant. The middle cell is optimized for each top cell/bottom cell combination. Cells are connected in electrical series.

gap of close to 1 eV [29]. While this substantially improves the combination of band gap values available at this lattice constant, the material must be grown by the more expensive and slower molecular beam epitaxy process rather than conventional metalorganic chemical vapor deposition (MOCVD) [29].

Were a substrate with tunable lattice parameter available, it would facilitate growth of MJSCs with more optimal band gap combinations and fewer internal electrical defects. These factors combined could result in a substantial improvement in efficiency over current MJSC record devices. Chapter 3 details a concept for a "virtual substrate", a growth template where the lattice constant can be specified, and presents experimental results on fabrication. Figure 1.8 shows the detailed balance efficiency of potential triple junction designs constrained such that all sub-cells are lattice matched to one another at lattice constants intermediate to InP and GaAs. The peak efficiency corresponds to a lattice constant of 5.80 A, which identifies a target lattice constant for virtual substrate fabrication efforts.

1.7 Overview of thesis

Chapter 2 of this thesis develops the detailed balance calculation in more detail and identifies two additional parameters that can capture a large amount of non-ideal solar cell behavior. This modified detailed balance approach is then used to identify optimal band gap combinations for solar cell ensembles with 2 to 20 sub-cells. The expected performance of these ensembles is compared under different material quality scenarios and combined with realistic optical and electrical losses to identify design strategies that could achieve system efficiencies of 50% or higher.

Chapter 3 of this thesis presents the results of experimental efforts to fabricate epitaxial growth templates for lattice-matched MJSCs. This "virtual substrate" concept consists of a template allowing epitaxial growth at any desired crystal lattice constant without requiring metamorphic growth. Efforts focused on creating templates of InGaAs with a lattice constant of 5.80 A to enable growth of a lattice-matched triple junction MJSC with high theoretical efficiency.

Chapter 4 examines the radiative emission from a solar cell as a loss mechanism and the possible efficiency gains from recovering that radiation for conversion in a different sub-cell of an ensemble. While some amount of radiative emission is inevitable, it is possible to alter the amount somewhat. The rate of internal recombination is a function of the chemical potential, but once a photon is emitted internally, it might either be reabsorbed or escape the cell. Designing the cell optical environment to direct radiated photons to other sub-cells in an ensemble can improve overall system efficiency. Taking the radiative coupling of sub-cells into account when choosing the band gap values of the sub-cells can yield further efficiency improvements.

Chapter 5 analyzes the annual energy production potential of the ensembles optimized in Chapter 2. By incorporating average atmospheric conditions into a multiple scattering and absorption model of the atmosphere, the degree of spectral variation over the course of a day and year for multiple different locations is analyzed. These spectra are then used as the input for detailed balance performance calculations for spectra splitting ensembles with 2 to 20 sub-cells and with both electrically in-

series and independent sub-cells. The expected annual energy production for these ensembles is calculated and analyzed.

Chapter 2

Spectral splitting strategies for ultra-high efficiency

2.1 What is spectral splitting

Spectral splitting is the concept of dividing the solar spectrum among multiple sub-cells with different band gaps to minimize thermalization and transmission losses [30, 31]. Because a single-junction solar cell loses 67% of the energy in the incident spectrum to the combination of transmission and thermalization [13], spectral splitting is a straightforward way to increase conversion efficiency while still using conventional photovoltaics .

2.1.1 Spectral Efficiency

The potential benefit of spectral splitting and the fine-ness of sub-bands required to achieve various efficiency targets can be understood to first order by examining the spectral efficiency of an ensemble. This thesis defines the spectral efficiency of a solar cell in Equation 2.1. All photon energy in excess of the band gap, Eg, is considered waste in this definition, as is the energy of photons lost to transmission.

$$S.E. = \frac{\int_{Eg}^{\infty} Eg\mathrm{AM1.5D}dE}{\int_{0}^{\infty} E\mathrm{AM1.5D}dE} \tag{2.1}$$

In an ensemble of sub-cells, the photons with energy below the lowest sub-cell band gap are lost, and the ensemble spectral efficiency will be no greater than the average (weighted by photon) spectral efficiency of the various sub-cells, as shown in

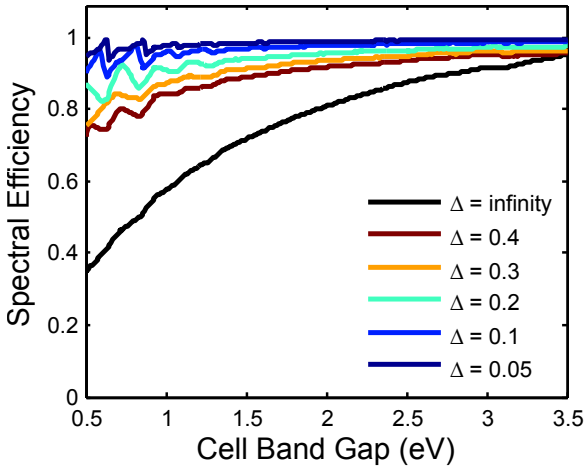

Figure 2.1. Spectral efficiency of a single junction cell exposed to spectral sub-bands of different energy width. In this case, the spectrum is truncated at the cell band gap value to eliminate losses due to transmission.

Equation 2.2.

$$S.E. = \frac{\sum_{Eg_1}^{Eg_n} \int_{Eg_i}^{\infty} Eg_i \mathrm{AM1.5D} dE}{\int_0^{\infty} E \mathrm{AM1.5D} dE} \tag{2.2}$$

Figure 2.1 shows the spectral efficiency of a single sub-cell exposed to sub-bands of the AM1.5D spectrum of varying width, δ as the band gap of the sub-cell varies. The spectral efficiency of a sub-cell exposed to the complete spectrum above its band gap is also plotted for comparison. In this plot, transmission losses are neglected due to the assumption of the presence of additional sub-cells. This figure shows that spectral efficiency for any delta rises with sub-cell band gap, which is expected. The features in the curves between 0.4 and 1.1 eV correspond to molecular absorption bands in the AM1.5D spectrum, where there are few photons available. The plot indicates that achieving a high average spectral efficiency will require very narrow sub-bands in the lower energy ranges of the spectrum, while wider sub-bands can be tolerated at higher energies.

2.1.2 Spectral splitting approaches

There are two practical approaches to spectral splitting. The most common embodiment of spectral splitting is in monolithically stacked multijunction solar cells (MJSCs), which consist of two or more sub-cells grown one on top of the other, with the highest band gap cell exposed to the incident light [13, 14]. The spectral splitting is accomplished by sequential absorption of the sub-bands as they pass through the sub-cells. Each sub-cell absorbs the photons with energy greater than or equal to the cell band gap value and transmits the remaining photons to the sub-cells below, until all photons are either absorbed or lost through transmission through the entire ensemble. In general, the monolithic integration makes it impractical to make electrical contact to each sub-cell individually, so the sub-cells are connected in series electrically by means of tunnel junctions grown between the sub-cells [16]. As a consequence of the electrical series connection, all sub-cells must pass the same amount of current, and so for efficient performance, all sub-cells must absorb the same number of photons. The need to split the spectrum into different sub-bands with the same number of photons constrains the combination of band gaps for an optimal MJSC.

Alternatively a separate optical element can divide the spectrum and direct it onto an array of physically isolated sub-cells[30]. This concept has the advantage of allowing band gap combinations that are not constrained by series connection requirements or the demands of monolithic crystal growth. The cost of this freedom is the need to construct a separate optical system to accomplish the spectral splitting.

It is quite possible to combine the two approaches and construct a system that incorporates an optical element for spectral splitting and uses MJSCs as one or more of the sub-cells in the array [32]. The merits of such a system would be highly dependent on the specifics of the optical system and the band gap combinations selected for the sub-cells. This thesis restricts its analysis to systems with sub-cells that are either completely series-connected or completely independent electrically. In both cases it is assumed that an optical system is present to concentrate and/or split the spectrum as needed, but the details of that system are left for future development. This work

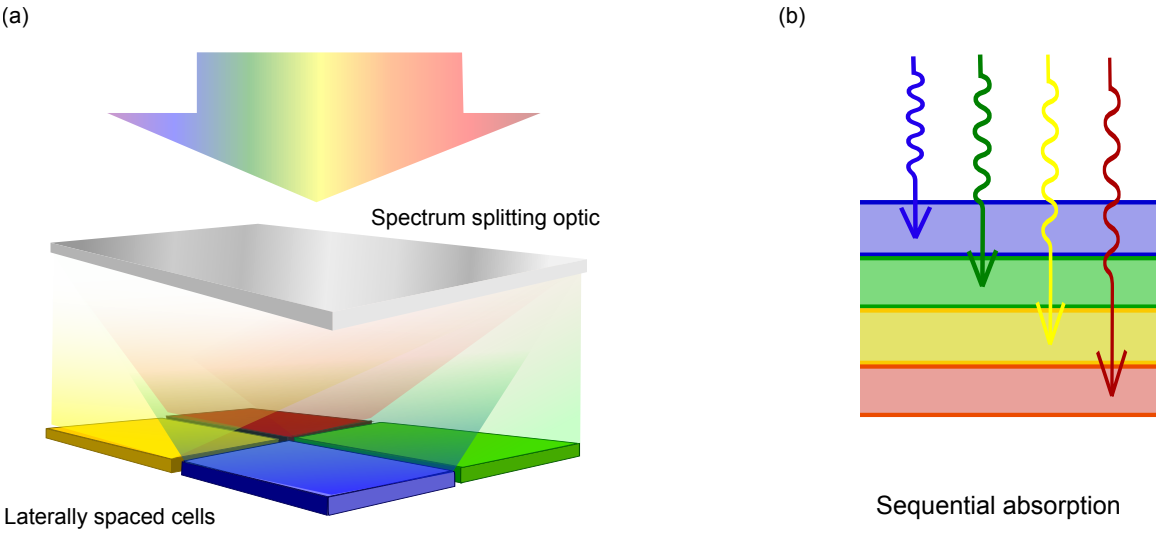

Figure 2.2. Conceptual drawing contrasting (a) spectrum splitting where a separate optic is used to distribute different sub-bands of the incident spectrum onto isolated sub-cells and (b) monolithically integrated MJSCs where the spectrum is split through sequential absorption.

is an exploration of the design strategies for the ensemble of sub-cells in spectrum splitting in pursuit of ultra-high efficiency.

2.2 Optimizing spectra splitting ensembles

While the efficiency limits of spectrum splitting ensembles with an infinite number of sub-cells are well defined, the benefit of adding sub-cells to systems with a small number of sub-cells has not yet been thoroughly explored. One challenge is the difficulty of optimizing the combination of band gaps for these ensembles. When the sub-cells are electrically in-series, the requirement that each sub-cell absorb an equal number of photons provides a constraint to the design space, and the optimization can be done through a direct comparison of all possible current-matched band gap combinations for a particular number of sub-cells. The band gap combinations that are current-matched are determined from a simple numeric integration of the incident spectrum (in photons/cm^2-eV) [33], and the number of possible combinations is

small regardless of the ensemble size. The efficiency of each candidate ensemble is determined through a detailed-balance calculation that enforces the current-matching condition on the sub-cells and simulates the J-V behavior of the monolithic stack. Radiative coupling between the sub-cells was neglected for this optimization.

2.2.1 Simulated Annealing

Optimizing the combination of band gaps for the ensembles with electrically independent sub-cells presents an additional challenge. Without the requirement that each sub-cell absorb the same number of photons, the design space grows exponentially with the number of sub-cells in the ensemble. Performing a full combinatorial comparison of possible designs is computationally intractable for ensembles with more than 6 or 7 sub-cells. For the larger ensembles, the band gap combinations were optimized through a Monte Carlo technique termed "simulated annealing". The optimization tests sample candidate designs starting with a randomly generated seed design. At each step of the optimization, a new candidate is generated by randomly perturbing the current best design. If the performance of the new candidate exceeds the current best performance, the candidate is adopted as the new best design and forms the basis for the next step of the optimization. To help ensure that the full design space is sampled adequately, simulated annealing allows an inferior candidate can be adopted as the new basis for perturbation in the next optimization step, if the deficit between the performance of the best design and the candidate is smaller than some threshhold value. Typically, the threshhold for adopting a lower-performing candidate narrows as the optimization progresses, and the name "simulated annealing" comes from the similarity of this gradual restriction to the cooling temperature of an actual annealing process.

To find a global optimum, the simulated annealing algorithm must be able to search the entire design space widely in the early steps, which requires the random perturbations that generate new candidates to be large. The criteria for accepting a lower-performing candidate as the base for further perturbation must also be loose enough for a high percentage of early-stage candidates to pass the test. Ideally the

early stages of the process will identify the region of the design space that contains the global optimum. At later stages of the optimization, it is preferable that the algorithm search the more restricted portion of the design space around that global optimum. The tightening threshold (analogous to a decreasing annealing temperature) is intended to serve this purpose and allow the random sampling to find the top of the performance peak without restricting the magnitude of the random perturbations applied to the design at every step of the optimization. Ideally the optimization will be repeated multiple times and result in the same optimum. This does not prove that the optimum is the true global optimum, but it is a necessary condition.

In optimizing the band gap combinations for the electrically independent spectrum splitting ensembles, the design consisted of the set of n band gap values for an n-cell ensemble. The perturbation was a set of n band gap deviations, with each deviation randomly sampled from a normal distribution centered on zero and with a standard deviation that varied with the size of n. At each step the base ensemble of band gaps was perturbed and then re-ordered in ascending value, as ensembles with non-monotonically increasing band gap value are not considered valid designs. The detailed balance efficiency of each design was calculated and that value compared to the efficiency of the current champion, and the new base for perturbation selected.

Initial attempts at optimization were unsuccessful at achieving repeated optimum values and often returned designs with obviously non-optimal features (such as band gap separations that were too small or too large). In many cases the best performing design was effectively equivalent to an ensemble with fewer sub-cells due to one sub-cell being starved for current. Apparently the large perturbation required to sample the design space effectively created a low probability of perturbing a high-efficiency design to an optimal one. To solve this, a second round of simulated annealing was added to the optimization process. The second round used the first round best design as the seed and used a much narrower perturbation. The threshold for adopting a lower-performing candidate as the base for perturbation was also much higher. With the addition of this second round of annealing, the optimization was able to produce repeated optimum designs for spectrum splitting ensembles with independent

electrical connection and 2 to 20 sub-cells.

2.2.2 Optimized efficiency of spectral splitting ensembles

Figure 2.3 shows the detailed balance efficiencies of optimized spectral splitting ensembles with 2 to 20 sub-cells at different concentration values. Also plotted is the spectral efficiency of the electrically independent ensembles. The plot shows the increase in efficiency with increasing number of sub-cells is closely correlated with the increase in spectral efficiency, which suggests that most efficiency gains are due to reduced thermalization and transmission losses. The increase in efficiency is most dramatic (17 percentage points) up to 8 cells, with only 4 percentage points of efficiency gained by increasing from 8 to 20 cells. Achieving a spectral efficiency of 90% requires an ensemble of at least 8 cells. Finally, the dashed lines for the series-connected spectral splitting ensembles are consistently 1-2 percentage points lower than those for the independently connected designs. This is a consequence of the current matching constraint forcing the selection of band gap combinations with a lower spectral efficiency.

Figure 2.3 also shows that increasing the concentration on the system from 1 sun to 1000 suns results in approximately 10 percentage points in efficiency improvement. Current record efficiency photovoltaic systems use concentration both to increase efficiency and to decrease the amount of solar cell area required in a module [29]. Concentration improves efficiency for solar cells by increasing the ratio of the short circuit current to the dark current, which increases the open circuit and operating voltages of the device [6]. If ultra-high efficiency is one of the design goals for a system, then increasing the concentration is a valuable design tool.

2.3 Modifying the detailed balance calculation

The efficiencies in Figure 2.3 suggest that 50% efficiency can be exceeded by a four cell ensemble at any concentration. However, these efficiency limits assume ideal behavior for photon absorption and radiation and perfect carrier collection. Practical

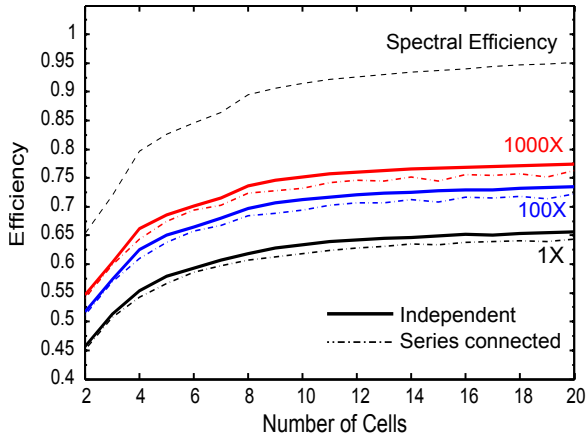

Figure 2.3. Detailed balance efficiency for ideal spectrum splitting ensembles with 2 to 20 sub-cells. Ensembles with electrically independent sub-cells are shown in solid lines, and electrically in-series ensembles in dotted lines. The spectral efficiency of the electrically independent ensembles is plotted as well.

cells will have less than ideal absorption due to reflection and transmission losses and will have some non-radiative recombination due to material imperfections. A more realistic model is required for identifying concepts that can achieve ultra-high efficiency in practical implementation. A device physics simulation can account for the specific material properties and design parameters of each sub cell [34], but it is computationally prohibitive to perform such simulations for each of the many cells considered in the optimization process. Instead, non-ideal material behavior can be incorporated into the detailed balance calculations through the introduction of two parameters: absorption efficiency and the external radiative efficiency, or ERE. The absorption efficiency modifies the short circuit current of the cell. This accounts for losses due to parasitic absorption by free carriers or in dead regions of the cell, reflection losses from the cell's top surface and for transmission losses due to finite cell thickness. The ERE is the percentage of internal carrier recombination events that result in an externally emitted photon, allowing the incorporation of non-radiative recombination losses into the detailed balance calculations [35, 36]. The cell's open circuit voltage decreases with non-unity ERE, as does the fill factor. Together, the absorption efficiency and ERE can account for the most common loss mechanisms in

high quality solar cells.

The advantage of this approach is that it retains the computational simplicity and speed offered by the detailed balance and therefore allows an extensive search of the design space. However, there is a real risk of misrepresenting the realistic non-ideal behavior of possible cells. The absorption efficiency and ERE are affected by both the material quality of a cell and the design specifics of that cell. For example, the absorption efficiency can typically be increased by increasing the thickness of a cell, by improving the anti-reflection coating on its top surface and by decreasing the optical thickness of any window or passivating layers. However, practical cells may have limits on these aspects of the design due to cost or material availability. Furthermore, changing the cell thickness and passivating layers may reduce the cell's ERE. The specifics of the interaction between absorption efficiency, ERE and material quality will not be constant over the entire range of materials and band gap values under consideration for spectrum splitting designs, but average or representative values can be used.

2.3.1 Device physics simulations for ERE and absorption efficiency

While there are experimental values for ERE and absorption efficiency for solar cells made from some of the materials under consideration, there are not enough data to generate a realistic average value for these parameters. The values from literature were augmented with a series of device physics simulations of solar cells made from five materials that span a large range of band gap values. The simulations were restricted to one dimension and performed on candidate designs of cells made from these materials using Afors-Het[34], a free device physics simulation tool built for photovoltaics. We incorporated realistic doping-dependent mobility and lifetime data for the candidate materials [37, 38, 39] to optimize device designs for each cell, including doping and thicknesses for emitter, base, front and back window layers and contact layers. The design parameters and efficiency results for these simulations are

Cell Band Gap	Composition	Ideal Voc (V)	Ideal Jsc (mA)	ideal FF	Voc (V)	Jsc (mA)	FF	ERE	Absorption	Source
0.74	$In_{0.53}Ga_{0.47}As$	0.3999	6.68	0.7718	0.388	5.91	0.7641	5.06%	0.888	model
0.94	$In_{0.71}Ga_{0.29}As_{0.62}P_{0.38}$	0.5946	8.57	0.8271	0.548	8.46	0.7886	1.60%	0.932	model
1.15	$In_{0.87}Ga_{0.13}As_{0.28}P_{0.72}$	0.7977	9.75	0.8608	0.751	9.23	0.831	1.20%	0.94	model
1.42	GaAs	1.154	32	0.8946	1.107	29.43	0.8757	22.50%	0.92	[19]
1.8	$Ga_{0.52}In_{0.48}P$	1.506	19.7	0.914	1.458	16	0.887	8%	0.816	[24]
2.13	$Al_{0.20}Ga_{0.32}In_{0.48}P$	1.7333	6.13	0.9242	1.64	5.77	0.8882	0.19%	0.945	model

Table 2.1. Ideal and realistic performance for candidate spectrum splitting cell materials as obtained by device physics simulations or literature sources. The ERE and absorption values corresponding to cell Voc and Jsc are shown.

summarized in Table 2.3.1. In all cases the simulated efficiency of each cell was substantially lower than the ideal detailed balance efficiency, as expected. However, the lowest band gap cells exhibited the largest departure from the ideal efficiency. This trend suggested the need to re-optimize the band gaps for the ensembles to account for realistic material behavior. Table 1 also includes the ERE values extracted from the simulated device performance parameters for each cell material [36] and the absorption efficiency, which is the short circuit current as a percentage of the value predicted by detailed balance. The values for the GaAs and InGaP cells are taken from record cell performance reported in the literature [19, 36].

The ERE values in Table 2.3.1 vary over a wide range among the cells. Because the cell open circuit voltage decreases linearly with the natural logarithm of ERE, a direct average of ERE values will overstate the expected average performance of these cells. Instead, taking the average of the natural log of the ERE values results in an average ERE of 3%. The performance of an ensemble of cells with these band gaps and that average ERE value will have the same total efficiency as the ensemble with the cell-specific ERE values. While this value is higher than the simulated value for most of the cells, the highest ERE values included in the average come from experimentally realized cells, suggesting that optimization of growth and other device parameters can produce III-V devices with very high radiative efficiency. The mean of the absorption efficiency values is 90.6%. For simulation purposes the value 90% was chosen as a conservative yet realistic de-rating value.

2.3.2 Efficiency under modified detailed balance

It is straightforward to incorporate these ERE and absorption efficiency parameters into the detailed balance calculation, as shown in the following equation

$$J(V) = \left[abs \int_0^\infty AM1.5DdE - \frac{1}{ERE} \frac{n^2 sin^2\theta_c}{4\pi^2\hbar^3c^2} \int_{E_g}^\infty \frac{E^2}{e^{(E-qV)/k_BT} - 1} dE \right] \quad (2.3)$$

where n is the cell index of refraction, θ_c is the emission angle of the cell and AM1.5D is the flux density per eV of the standard spectrum. Again, the modified equation balances the incident flux as modified by the absorption efficiency (abs) with the collected carriers and the radiative and non-radiative recombination. The cell's radiative emission is assumed to follow the same Kirchhoff relation as in the unmodified calculation [9], but that quantity is now assumed to be a percentage equal to the ERE of the total recombination. With these assumptions we calculate a new J-V relation for each cell and determine its fill factor and maximum power point under illumination by its particular spectral slice. Note that we assume unity absorptivity for photons with energy at or above the cell's band gap value, and zero absorptivity for lower energy photons. This allows us to disregard the cell's thickness in these calculations.

Including non-unity ERE and absorption efficiency did not change the optimal band gaps for the series-connected ensembles. The constraint of in-series electrical connection and the need to maximize spectral efficiency dominate the sub-cell band gap selection regardless of material quality. However, the band gaps for the independently connected designs did change upon the inclusion of non-ideal material behavior. The designs of ensembles with fewer than 10 cells exhibited the strongest dependence on material quality. Once optimized with non-unity ERE and absorption efficiency, the electrically independent designs uniformly increased the band gap energy of the lowest energy sub-cell. This trend is a result of low band gap cells being particularly sensitive to decreases in ERE. At low band gap energies the loss of voltage due to non-unity ERE consumes a greater percentage of the open circuit voltage, and the

fill factor also degrades more significantly, which combine to eliminate the benefit of capturing more low energy photons. Ensembles with more than 10 cells did not have large changes in sub-cell band gap values after optimization with non-ideal material parameters. The expected efficiencies with 3% ERE and 90% absorption efficiency are 10 percentage points lower than the ideal detailed balance efficiencies.

2.4 Systems that can achieve ultra-high efficiency

While the modified detailed balance approach gives a realistic prediction of the efficiency of an ensemble of cells, the total system has additional losses that must be taken into account. A practical spectrum splitting photovoltaic system will require some optical system to split and concentrate the incident spectrum into the desired spectral range for each sub cell in the design. Such a system will inevitably introduce inefficiency through misallocation of photons to the wrong cell and internal and external reflections. In addition, an electrical system to combine the power of the sub-cells at a single output voltage will add electrical losses. In order to accommodate these optical and electrical losses and still produce system efficiency greater than 50%, the ensemble of sub-cells must have a combined efficiency of much greater than 50%. Figure 2.4 shows the two-dimensional plot of efficiency versus number of cells and concentration for independently connected systems with 2 to 20 sub-cells. The two panels of the figure show the cell ensemble efficiency under two different material parameters: (a) 3% ERE and 90% absorption efficiency, and (b) 5% ERE and 90% absorption efficiency. Marked on each plot are contours showing total system efficiency with a spectrum splitting optic with 90% optical efficiency and electrical system of 95% efficiency.

These plots show the importance of ERE for achieving a high system efficiency. With the lower external radiative efficiency, it requires at least 7 sub-cells at a concentration of 560 suns to achieve a total system power conversion efficiency of 50% with 90% efficient optics and 95% efficient electronics. By contrast, the set of designs with 5% ERE and 90% absorption efficiency can achieve 50% system efficiency

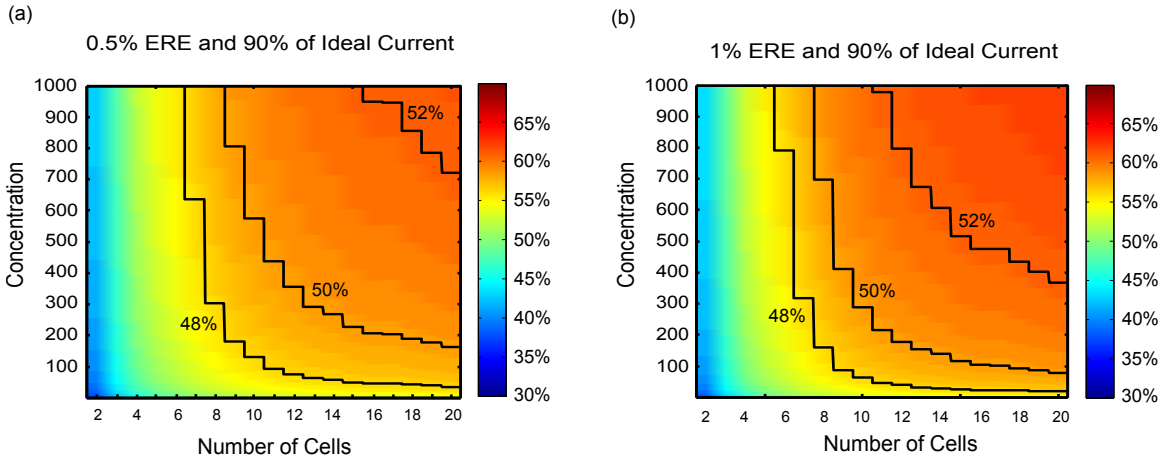

Figure 2.4. Efficiency of independent ensembles with different numbers of sub-cells at different concentrations for (a) 3% ERE and 90% absorption, and (b) 5% ERE and 90% absorption. The contours plot the required concentration and cell number required to achieve different overall system efficiency levels given 90% optical and 95% electrical system efficiencies.

with realistic optical and electrical losses using a design with 6 sub-cells at 841 suns concentration. The concentration required decreases with larger numbers of sub-cells, and only 59 suns are required to achieve 50% system efficiency with 10 sub-cells. This highlights the trade-off in complexity between the optical design and the cell design in achieving very high system efficiency.

Figure **??** presents another view of the interaction between number of cells, concentration and ERE in determining overall system efficiency. This plot shows the efficiency of independently connected cell ensembles at 10 suns and 500 suns concentration with different ERE values. The contours again show total module efficiency with 90% efficient optics and a 95% efficient electrical system. Considering first panel (b), the plot at 500 suns concentration, at 1% ERE, this plot indicates that 9 sub cells will be required to achieve 50% module efficiency. The steepness of the contours in the region from 4 to 10 cells highlights the value of improvements in ERE. An increase from 1% to 2% ERE reduces the number of sub cells required to achieve 50% from 9 to 8, which would constitute a significant reduction in potential cost and

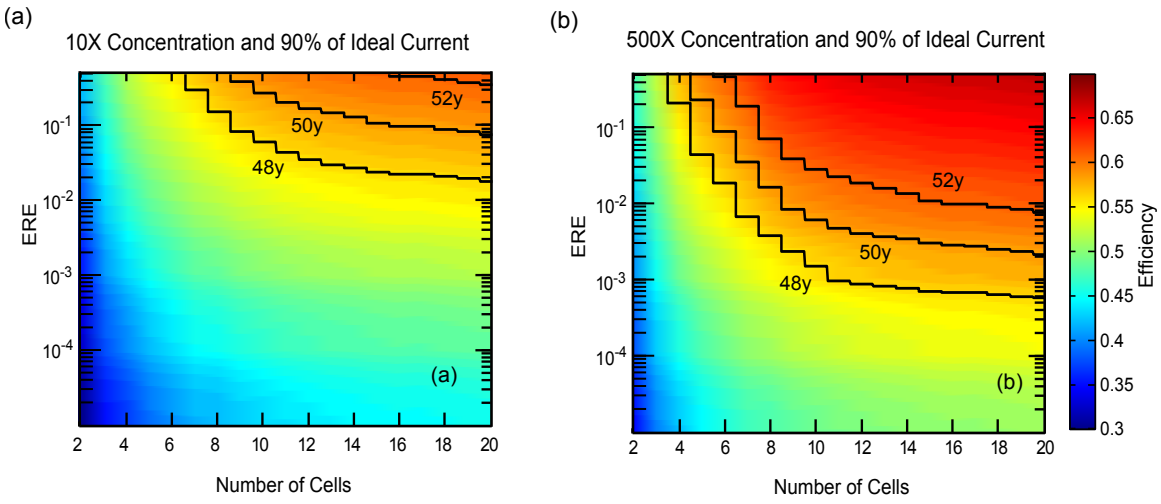

Figure 2.5. Efficiency of independent ensembles with different numbers of sub-cells at different ERE values for (a) 10X concentration and 90% absorption, and (b) 500X concentration and 90% absorption. The contours plot the required concentration and cell number required to achieve different overall system efficiency levels given 90% optical and 95% electrical system efficiencies.

complexity. By contrast, the plot for 10 suns shows that low concentration systems will require 10 or more cells with average radiative efficiency equal to current record performance devices.

Figure **??** and **??** also indirectly highlight the challenge of achieving very high system efficiency with series connected cells. As Figure 1 showed, series connection reduces the efficiency of an ensemble with a given number of cells by 1.5 to 2 percentage points. This means such a system will require either a much higher concentration (100 to 300 additional suns) or a larger number of cells to achieve a comparable performance. The series-connected ensemble could recover some marginal advantage due to the need for a simpler electrical system, but increasing the electrical system efficiency from 95% to 97% only recovers one third of the efficiency handicap. Therefore, while series connection may allow for simpler cell integration and electrical configuration, it is not a practical design approach for exceeding the 50% efficiency target.

2.5 Chapter conclusion

Achieving ultra-high system efficiency (50% or greater) for photovoltaic solar conversion requires a combination of a large number of high quality cells, an efficient optical system to split the incident spectrum correctly among those cells and a moderate to high degree of concentration. The radiative quality of the cells will determine the optimum band gaps of the cells in an ensemble and the radiative and absorption efficiencies together determine how far the cell performance departs from the ideal detailed balance limit. By including these two parameters into the detailed balance calculation, we have predicted that a system efficiency of 50% or greater will be possible with 7 to 10 electrically independent cells in a spectral splitting optic at 300 to 500 suns concentration, assuming a 90% optical efficiency and 95% electrical efficiency.

Chapter 3

A virtual substrate for conventional monolithic MJSCs

This chapter details experimental efforts to fabricate templates for improved monolithic MJSCs as part of the effort to achieve ultra-high efficiency solar cells. As described in chapter 1, current record efficiency cells are series-connected triple-junction cells grown in a monolithic stack [12, 14, 29]. The sub-cells are connected in electrical series by means of tunnel junctions, and therefore all sub-cells will pass an equal amount of current. In an optimal design, all sub-cells will absorb the same number of photons and thus be able to operate at their maximum power point. If one sub-cell absorbs extra photons, most of that additional power will be lost. Conversely, if one sub-cell absorbs fewer photons than the others, its lower current will constrain the entire ensemble.

Optimizing a set of band gaps for equal spectrum splitting and efficient series-connected performance requires a set of materials that can be grown sequentially with high quality at the particular band gaps that allow equal current. In practice, high efficiency MJCSs are most commonly made using the III-V family of materials, and deposition occurs through epitaxial crystal growth by metalorganic chemical vapor deposition (MOCVD) or molecular beam epitaxy (MBE). Figure 3.1 shows the III-V family with the material band gap plotted versus lattice constant. The dots correspond to binary compounds, the curves to ternary alloys of the binary compounds at their end points, and the space enclosed by curves corresponds to quaternary alloys. This plot also includes the optimal band gap values for series-connected three and four junction MJSCs [33].

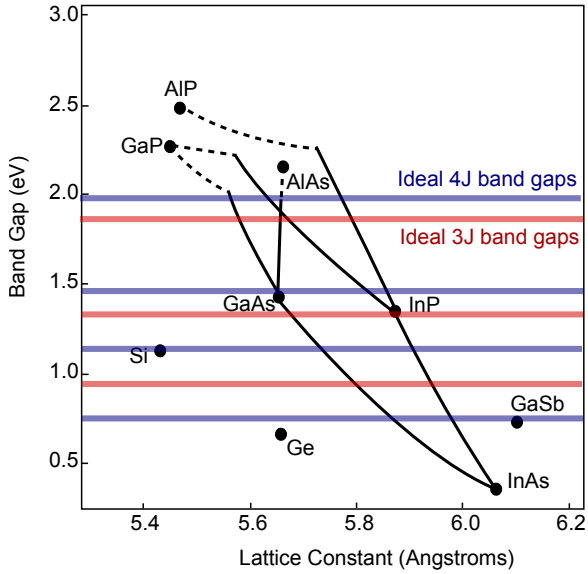

Figure 3.1. Band gap versus lattice constant for a subset of the III-V material family. Dots represent binary compounds, curves represent ternary alloys of their binary endpoints, and the space enclosed by curves consists of quaternary alloys. Elemental semiconductors silicon and germanium added for reference. The red lines indicate the optimal band gaps for a series-connected triple junction MJSC and the blue lines indicate the optimal band gaps for a series-connected four-junction cell.

Presently it is only possible to buy single crystal wafers of the binary compounds on this plot, as well as the group IV elemental semiconductors silicon and germanium, also shown on the plot. At the lattice constant of these wafer materials, it is not possible to grow lattice-matched MJSCs with three or four sub-cells and ideal band gap combinations with the materials shown on this map.

3.1 The need for better epitaxial templates

The lack of a single-crystal wafer substrate with a lattice constant that allows optimal band gap combinations limits the potential efficiency of MJSC designs. The best current lattice-matched concept uses a germanium substrate and germanium bottom cell [27]. This allows a lattice-matched GaAs middle cell and InGaP top cell. While the top and middle sub-cells are nearly current matched, the Ge bottom cell absorbs many more photons and adds less voltage to the ensemble performance than is optimal. The ideal limiting efficiency for this design (at 500 suns) is 50.5%, as compared to the optimal triple junction detailed balance efficiency of 57% [27]. The design gives up a lot of potential performance for the sake of lattice matched growth.

As figure 3.1 shows, there are lattice constants with available band gap combinations much closer to the optimal designs. Unfortunately, attempting to grow them on the available wafer substrates is unlikely to result in high material quality. Epitaxial growth uses the substrate crystal to serve as a template for deposition of the film crystal. As the atoms of the film material accumulate on the surface, they organize themselves in the lowest energy configuration possible. Initially this means a continuation of the substrate crystal structure at the substrate lattice constant, but with the film composition. If the film material has a different lattice constant than the substrate, the film crystal will distort to adopt the substrate lattice parameter in the plane of the growth surface, with a compensating distortion out of the plane to conserve the unit cell's volume [40]. This is shown schematically in Figure 3.2.

The distortion of the film's crystal results in strain energy, which increases with the thickness of the film. Once the film reaches a particular thickness, the energy required

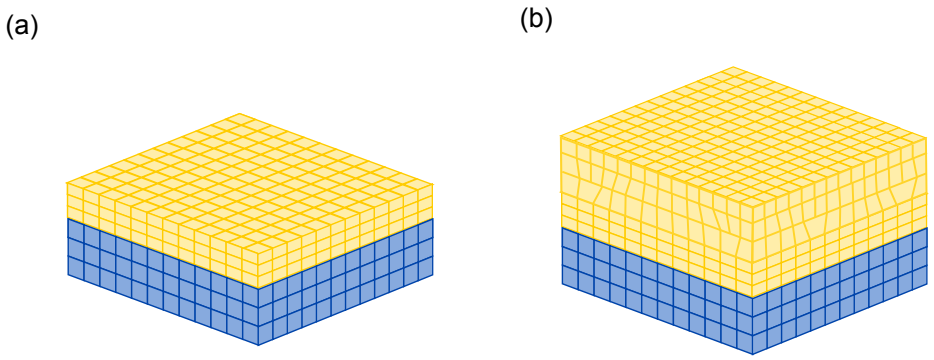

Figure 3.2. Conceptual drawing of dislocation formation in strained epitaxy. Initially (a) the film lattice distorts to match substrate lattice in-plane and deforms in the out-of-plane dimension to maintain unit cell volume. At some thickness, (b) it becomes energetically favorable to form dislocations and allow the film to take its natural lattice parameter in all dimensions.

to form a strain-relieving dislocation becomes less than the amount of strain energy reduced by the dislocation. This critical thickness, as determined by Matthews and Blakeslee [40], is plotted in Figure 3.3 for InGaAs films grown on InP substrates and InGaP films grown on GaAs. In both cases the critical thickness drops off rapidly as the lattice parameter deviates from the substrate, and it falls below the 1000 nm required for optically thick solar cells that can achieve good absorption of their designated photons.

The low critical thickness at lattice parameters far from that of the wafer substrate suggests that a thick film grown with significant lattice mismatch will contain a high density of strain-relieving dislocations. By disrupting the order of the crystal lattice, dislocations introduce electron states within the material's band gap that serve as centers for non-radiative recombination. High dislocation density will correspond to low quality in these materials and will degrade performance through reduced voltage.

In practice, the process of dislocation nucleation is kinetically limited, and therefore films can be grown much thicker than the critical thickness and remain under strain. At the low temperatures possible with MBE, it is possible to achieve film 100 - 200 nm thick despite composition-dictated critical thickness of 10 to 20 nm

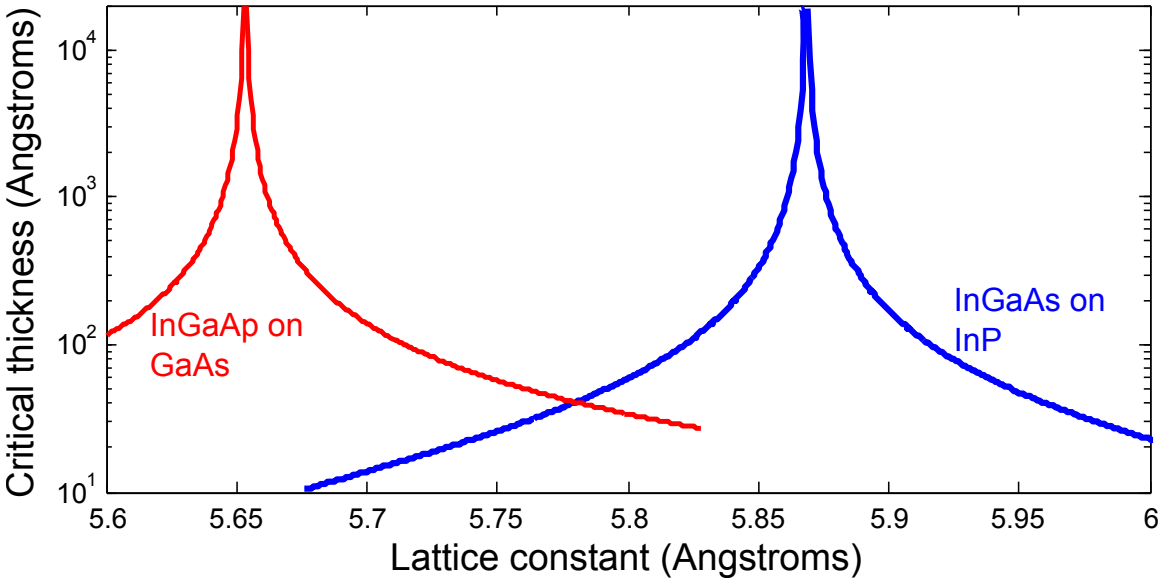

Figure 3.3. Matthews-Blakesly critical thickness of InGaP grown on GaAs and InGaAs grown on InP. In both cases the critical thickness decreases rapidly as the film's native lattice parameter diverges from the substrate lattice constant.

[41]. This thickness is still not sufficient for one optically thick solar cell, let alone a multi-cell stack. The MOCVD process requires higher growth temperatures, and consequently is even more limited in the ability to produce thick strained films. Growth of high quality material with a lattice constant different from that of the wafer substrate therefore requires some alternate strategy to manage or prevent dislocation nucleation.

3.1.1 Metamorphic growth

While dislocation formation is inevitable for thick films with different lattice parameter than the substrate, the final density of dislocations can be controlled to some degree [41]. By changing composition gradually and growing slowly, the amount of strain energy that each dislocation relieves can be maximized. This process of using compositionally stepped or graded buffers results in metamorphic growth, where most of the lattice strain is relieved and the film is close to its natural lattice parameter in all directions.

Top Eg	Middle Eg	Bottom Eg	Ideal efficiency	Experimental efficiency
1.9	1.42	0.67	50.5%	41.6%
1.84	1.32	0.67	54.5%	41.1%
1.84	1.32	1	53.4%	40.8%
1.9	1.42	1	53.0%	44%

Table 3.1. Band gap values and theoretical and record achieved efficiency for lattice matched and metamorphic triple junction MJSCs.

Metamorphic growth is a common strategy for MJSC designs with more optimal band gap compositions [28, 42, 43]. Eliminating the constraint that all band gaps in the design must be available at the same lattice constant expands the possible band gap combinations greatly. However, this freedom comes with the penalty of requiring a thick graded buffer for every new lattice constant included in the design. Further, the buffer must be designed to minimize parasitic absorption of light intended for the sub-cells below it, and the time required to grow the ensemble increases substantially with each buffer included. Optimizing the design for cell performance and cost may result in complicated manipulation of the structure, such as growing the ensemble upside down and removing it from its substrate or growing sub-cells on both the top and bottom of the wafer. Table 3.2 lists a few high-efficiency metamorphic designs and the experimental efficiencies achieved. While the theoretical efficiency of these ensembles is higher than that of the lattice-matched design, the observed performance is not much better. This suggests the dislocation density resulting from mismatched growth restricts the external radiative efficiency of these designs.

3.1.2 Dilute Nitrides

The collection of alloys shown on Figure 3.1 does not include all possible materials. Adding a small amount of nitrogen to the InGaAsPSb family of materials creates new alloys. In particular, there is a GaAsNSb alloy that is lattice-matched to GaAs and has a band gap of ĩeV [29]. Using this material as the bottom sub-cell allows lattice-matched growth of a GaAsNSb/GaAs/InGaP triple junction with a detailed

balance efficiency of 53.0% (at 500 suns). Cells with this design have achieved a record efficiency of 44% [29]. Unfortunately, this material is very sensitive to contamination during growth, and must be grown by MBE to achieve high quality. While incorporating dilute nitride materials into the design toolbox does extend the range of lattice-matched band gaps available on the GaAs substrate, the approach leaves the alloys at other lattice constants still inaccessible for cell designs.

3.2 Virtual substrate concept

High-quality epitaxial crystal growth requires only a few tens of nanometers of substrate crystal to establish the structure of the subsequent film. If such a thin crystal with the desired lattice constant were supported on a mechanical support to provide structural integrity, the combination would serve as a "virtual substrate" with all the same function as a single crystal wafer of the desired material. In order to function well as an epitaxial template, the film and handle substrate must be securely bonded to one another and able to withstand growth temperatures of 500 to 700 C. The film surface must be planar, smooth and free of defects. Further, the film itself must have a low dislocation density, preferably at least as low as the 10^3 per cm^2 commonly guaranteed by wafer suppliers. Finally, the film must be unstrained as it is bonded to the handle substrate. In order to serve as a template with the desired lattice constant, the film crystal must not be distorted.

This chapter presents a process for fabricating such a substrate and documents the results, including attempts to grow solar cell structures on "virtual substrates" with lattice parameters that are not available as single-crystal wafers [44].

3.3 Virtual substrate fabrication process

The virtual substrate is fabricated by removing a thin crystal film from its growth substrate and transfering it to a reactor-compatible handle such as a silicon wafer. The film composition is selected to provide the desired lattice parameter, and after

transfer the film is under no strain. The film is initially grown under strain on a wafer substrate, but the thickness is lower than the practical threshhold for dislocation nucleation. The transfer process must allow the as-grown strain in the film to relax elastically while maintaining a clean, atomically smooth, flat surface for bonding to the handle. The process is illustrated in Figure 3.4 below.

First, the film is grown elastically strained on a single crystal wafer substrate. As grown, the in-plane lattice parameter will be equal to that of the substrate, and the unit cell will be tetragonally distorted. Because the thickness is only 40 to 80 nm, no significant dislocation nucleation will occur even if the thickness is greater than the Matthews-Blakeslee critical thickness.

Second, a compliant wax handle is applied to the film. The wax is viscoelastic and will support the film while allowing the strain to relax elastically in subsequent steps.

Third, the film is removed from the growth substrate by chemical etching. In these experiments, the entire substrate thickness was removed through chemical etching. At this stage the film is supported only by the wax handle, and the strain relaxes, restoring the lattice to its native cubic configuration.

Fourth, the film, still supported on wax, is placed onto a silicon wafer with 100 to 300 nm of thermal oxide with a small droplet of water at the interface. Left for 24 hours, the water will evaporate and capillary force will draw the film into intimate contact with the handle wafer. If both surfaces are smooth to within approximately 1 nm, Van der Waals interactions will hold the film in place.

Finally, the wax handle is removed with solvent, leaving the film bonded to the handle and ready to serve as a template for subsequent growth.

3.4 Results of virtual substrate fabrication

The experimental effort resulted in fabrication of virtual substrates with size ranging from 1 cm2 to 12 cm2 and with lattice parameters ranging from 5.80 to 5.89 Angstroms. These templates all featured completely relaxed films bonded to silicon

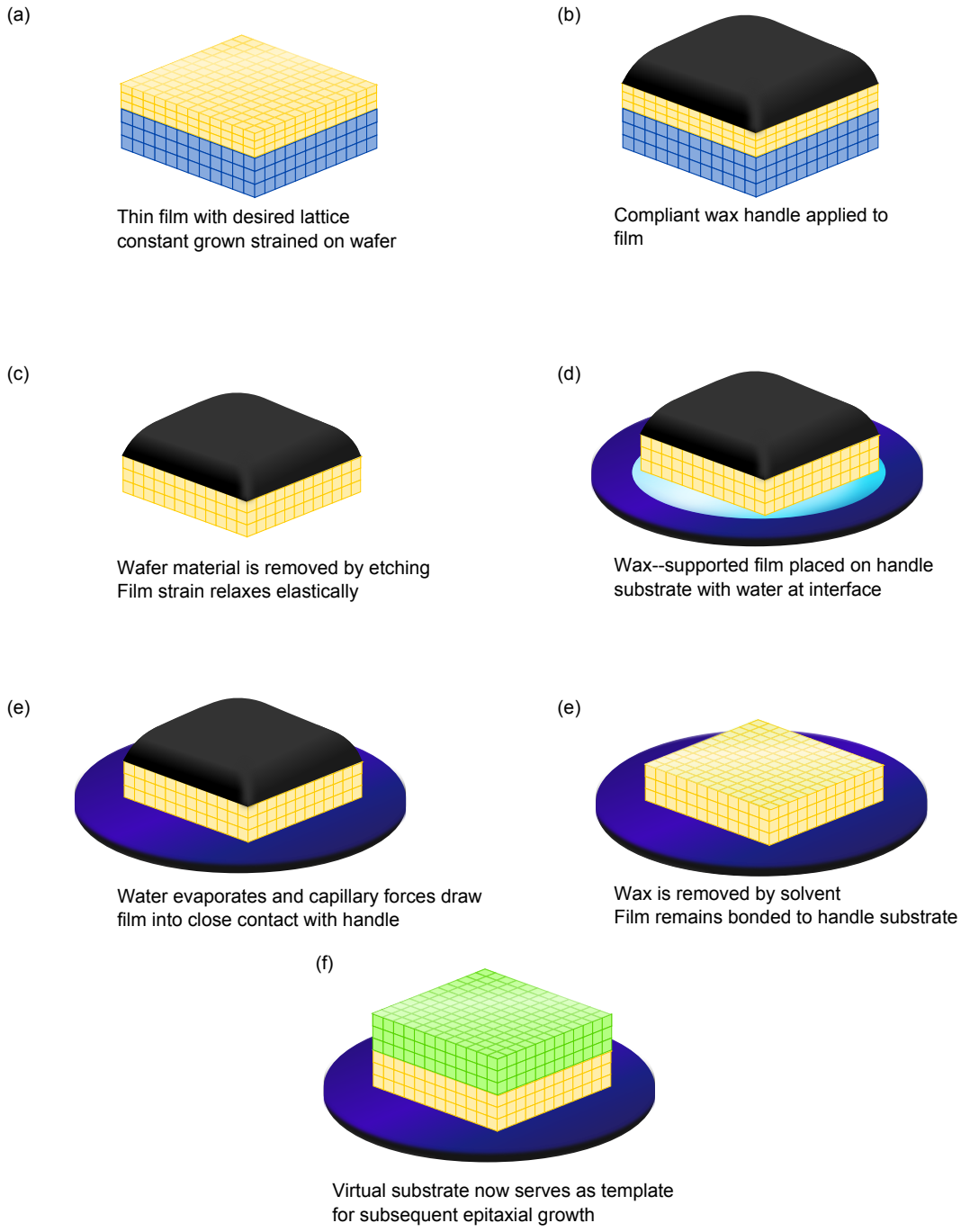

Figure 3.4. Fabrication steps for the virtual substrate.

wafers, as verified by x-ray diffraction. Attempts to grow solar cells on these substrates resulted in crystalline material of the desired lattice parameter, but of low optoelectronic quality.

3.4.1 Initial growth of strained layer

The first requirement for virtual substrate fabrication is a single-crystal film with the desired lattice constant and high quality. This film must be grown strained on an available wafer substrate to obtain lattice constants not currently available commercially. High crystalline quality requires a film thickness lower than the dislocation nucleation threshhold.

These experiments focused on two material systems: strained InGaAs films grown on InP wafers and strained InGaP films grown on GaAs. These ternary alloys can span the range of lattice constants between the 5.8685 Angstroms of InP and the 5.6325 Angstroms of GaAs. Lattice constants in this region correspond to a wide range of band gap values and have the potential to be suitable for MJSCs or other optoelectronic devices. In addition, in both of these material systems there are chemical etches with strong selectivity between the film and the substrate, which facilitates removing the film for transfer to the handle.

Table 3.2 lists the different film compositions grown, their substrate material, thickness, native lattice parameter, critical thickness, and degree of strain. Positive strain values correspond to tensile strain. The thickness of the InGaP films was chosen to be only 30 nm in order to accommodate the larger amount of strain in those films. The InGaAs films were grown at either 40 or 80 nm thickness. In most cases the film thickness was well excess of the Matthews-Blakeslee critical thickness. In all cases these films were grown by MOCVD by Sumika Electronic Materials.

The as-grown films were assessed for relaxation through high resolution x-ray diffraction (XRD) measurements, including symmetric and asymmetric rocking curves and reciprocal space maps. Figure 3.5 shows the (004) and (224) rocking curves of the 40 nm InGaAs film set, and Figure 3.6 shows the InGaP film set. The InGaAs films all show a strong, broad film peak, as expected for 40 nm thickness. The

Film material	Substrate	Strain	Critical thickness	Film thickness
In0.53Ga0.47As	InP	0	N/A	40 nm
In0.58Ga0.42As	InP	-0.30%	43	40 nm
In0.48Ga0.52As	InP	0.30%	38	40 nm
In0.45Ga0.55As	InP	0.50%	22	40 nm
In0.43Ga0.57As	InP	0.70%	17	40 nm
In0.43Ga0.57As	InP	0.70%	17	80 nm
In0.36Ga0.64As	InP	1.20%	9	80 nm
In0.43Ga0.57As	InP	0.70%	17	40 nm
In0.36Ga0.64As	InP	1.20%	9	40 nm
In0.62Ga0.38P	GaAs	-1%	11	40 nm
In0.70Ga0.30P	GaAs	-1.50%	6	40 nm
In0.72Ga0.28P	GaAs	-2.0%	4	40 nm

Table 3.2. Composition, mismatch and thickness for films grown for virtual substrate fabrication.

film is oriented along the same crystal axis as the substrate and the clear fringe pattern around the peak indicates smooth, high quality growth. In all cases the 004 plane spacing is as expected for perfectly strained films of the designed composition. Verifying the in-plane lattice spacing requires an asymmetric scan that probes lattice planes not parallel to the surface of the film. The 224 plane spacing is determined by both the in-plane and out-of-plane spacing. In combination with the information from the symmetric scan and the assumption of symmetry about the 110 direction, these measurements determine the dimensions of the unit cell and verify the film composition. The symmetry assumption can be tested by performing a second 004 scan with the sample rotated 90 degrees about the surface normal (or phi axis), which will detect any tilt angle between the film and substrate. Thus three simple measurements can verify the film composition, thickness and strain state.

As the scans in Figure 3.5 show, all the 40 nm InGaAs films were grown initially fully elastically strained, suggesting a low dislocation density. These films were judged

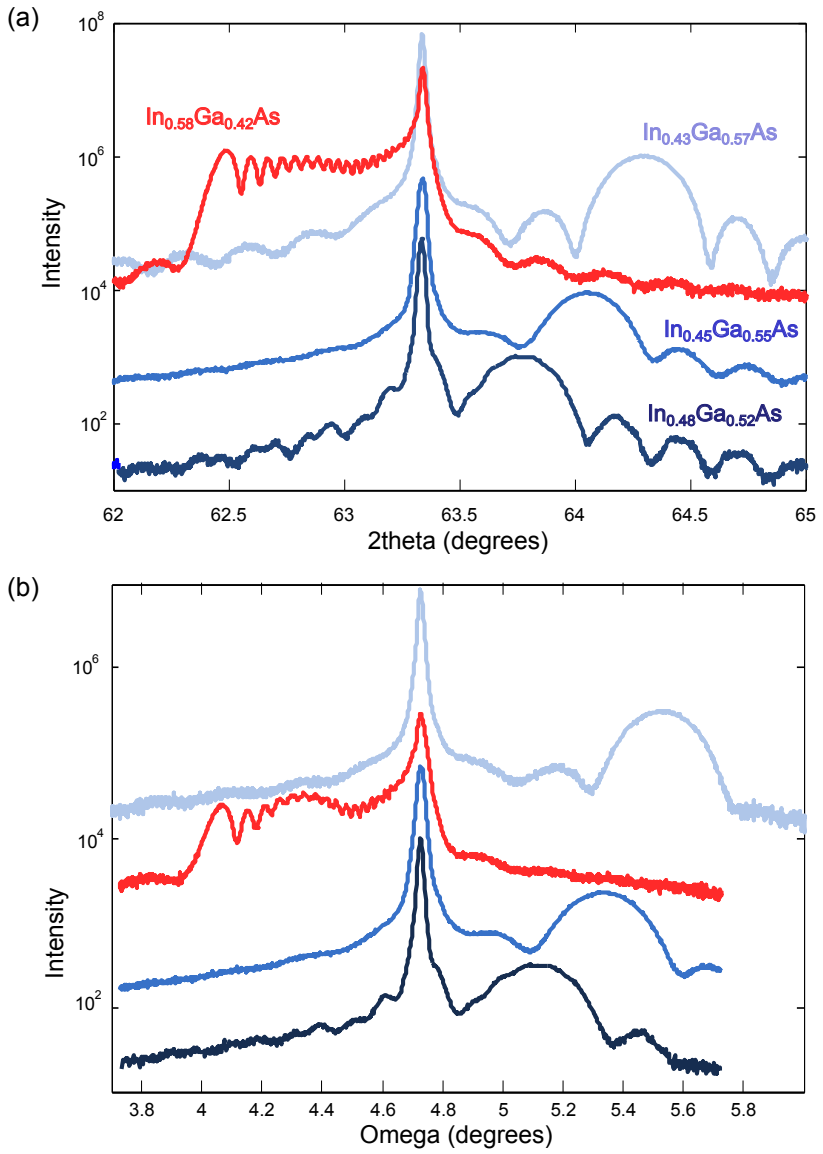

Figure 3.5. X-ray diffraction measurement of symmetric (004) peak and asymmetric (224) peak for InGaAs films grown strained on InP wafers for virtual substrate fabrication.

to be good candidates for transfer and virtual substrate fabrication.

The XRD scans of the InGaP films revealed lower quality material, as shown in Figure 3.6. Of the three compositions attempted, $In_0.72Ga_0.28P$ at -2.5% strain appeared to be completely relaxed. The 004 scan shows minimal fringes around the film peak, indicating thickness inconsistencies associated with a rough surface. Indeed, this sample appeared noticeably hazy relative to a pristine wafer or the InGaAs samples. The peak on the 224 scan is very low and broad, which can result from mosaicity or phase separation in the film. Regardless, this sample was judged inadequate for virtual substrate fabrication.

The intermediate InGaP composition, with 70% indium and -2% strain, exhibited partial relaxation. Approximately 30% of the lattice mismatch has been relaxed through dislocation formation. Finally, the least strained InGaP composition, with 62% indium and -1.5% strain, had low relaxation of 5%. While both of these materials are sub-optimal for virtual substrate fabrication, they remained in the experiment pool in order to broaden the range of lattice constants examined.

3.4.2 Film removal from growth substrate

Experiments with a variety of film removal techniques and transfer handle materials identified a few key requirements. First, the transfer handle material must be both soft and viscoelastic to allow strain relaxation in the film once it is removed from the substrate. The most successful handle was Apiezon W wax, a commonly used mounting wax soluble in trichloroethylene (TCE). The wax (technically a hydrocarbon mixture rather than a true wax) has a very high viscosity at room temperature and softens at 100 C, but remains very viscous. Both melting and solvent casting were viable application methods, but solvent casting enabled more consistent wax thickness and coverage, and was therefore the dominant method.

Experiments with Crystal Bond, another mounting wax that softens at 150 C and is soluble in acetone, were also successful when the wax was melted onto the sample. Because the performance of this wax was no improvement on the Apiezon W, it was not adopted. Attempts to transfer the films with a paraffin-based mounting wax, a

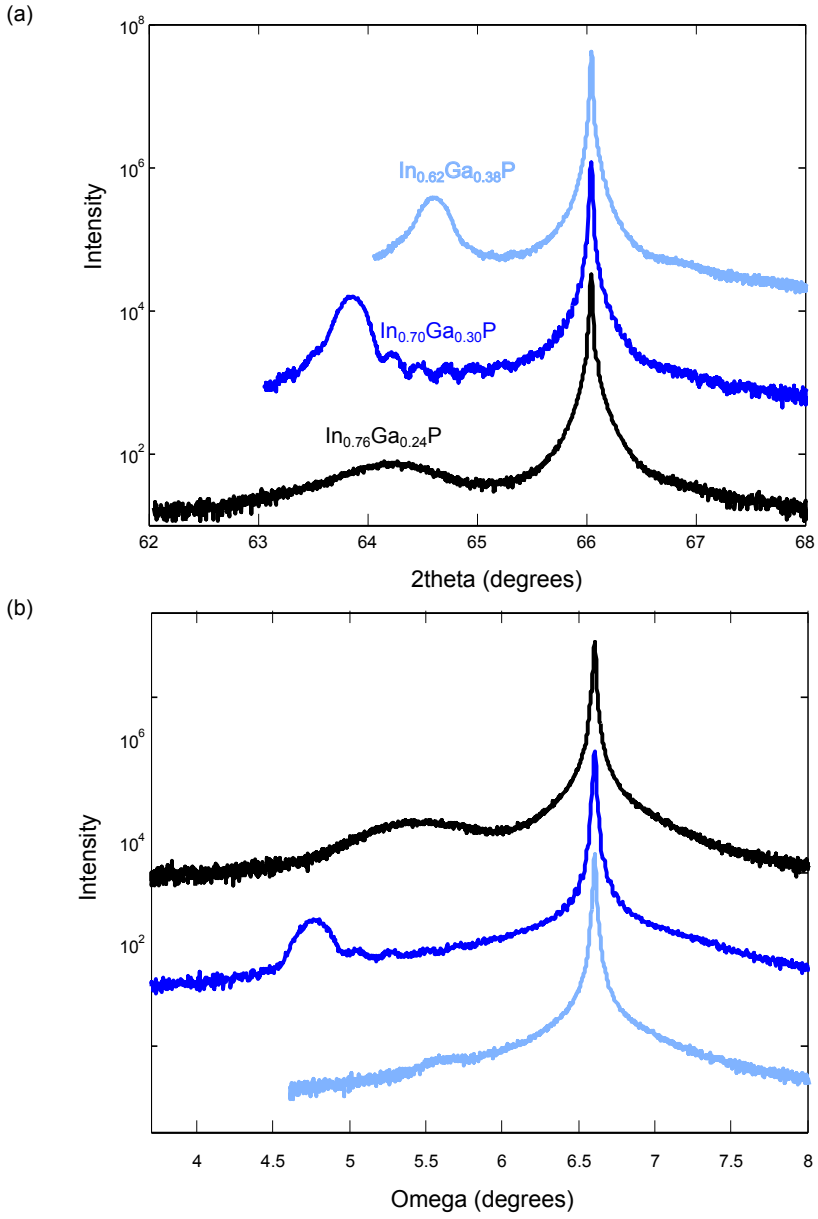

Figure 3.6. X-ray diffraction measurement of symmetric (004) peak and asymmetric (224) peak for InGaP films grown strained on InP wafers for virtual substrate fabrication.

true wax with a solid-liquid phase transition, did not result in strain relaxation in the film after substrate removal. This indicates that the viscoelastic nature of the transfer handle material is essential for allowing the film to relax to its native lattice parameter.

While the Apiezon W is quite hard at room temperature, the combined ensemble of a 40 nm film supported on 500 microns of wax is very delicate and sensitive to handling. Adding a secondary handle in the form of a glass coverslide or square of Kapton film was necessary to facilitate handling of the film during the etching transfer process.

The InGaAs films were freed from their substrates by a high-concentration HCl etch that completely removed the entire InP wafer. The HCl removed InP at 50,000 nm per minute and would reliably stop at the InGaAs surface, even in cases where the InP etched unevenly. The InGaP films were removed by etching a buried sacrificial AlAs layer 15 nm thick grown as part of the film structure with a 100 nm GaAs buffer separating the AlAs and InGaP layers. The thin GaAs buffer was subsequently removed by etching in a citric acid/H2O2 solution.

Once the films were removed from their growth substrates, they were rinsed in deionized water and dried with nitrogen. The films were bonded to silicon handle substrates with 100 to 300 nm of thermal oxide, by placing a droplet of deionized water on the silicon wafer and then placing the film - wax ensemble onto the water and pressing lightly to ensure a complete layer of water between the two surfaces to be bonded. The entire assembly was then placed in a fume hood for a minimum of 12 hours to allow the water to evaporate and capillary forces to draw the film into intimate contact with the silicon wafer surface. With the water evaporated, the wax was removed in TCE (or other appropriate solvent), leaving the film bonded to the handle through Van der Waals interactions. All wax residue was removed by rinsing in TCE, acetone, IPA and finally deionized water, and the completed virtual substrate dried with nitrogen gas. The bond between the film and handle substrate was strong enough to withstand these cleaning steps as long as all interface water had evaporated away and the film surface was sufficiently smooth.

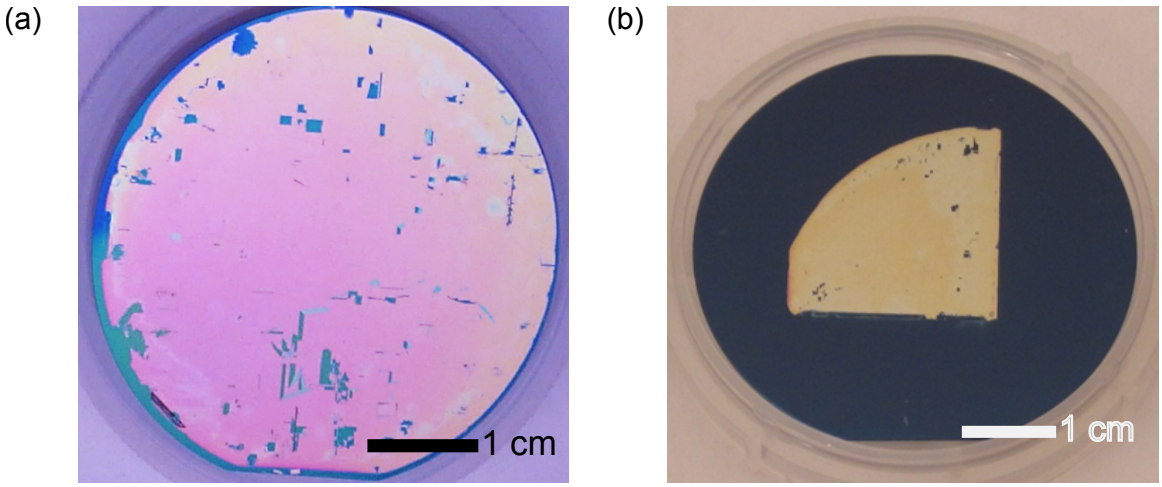

Figure 3.7. Photographs of virtual substrates consisting of 40 nm of InGaAs bonded to a silicon wafer with 300 nm of thermal oxide. Panel (a) shows a film with 43% indium and a lattice constant of 5.83 A, while the film in panel (b) is 36% indium at a lattice constant of 5.80 A.

Figure 3.7 shows photographs of a selection of virtual subtrates with the film composition and lattice constant indicated.

3.4.3 Film transfer to handle substrate

Once the virtual substrates were fabricated, high resolution x-ray diffraction (XRD) measurements were repeated to verify full film relaxation. Figure 3.8 presents the 004 scans of the InGaAs films as grown on InP and after virtual substrate fabrication. In all cases, the film peak shifts significantly after transfer, indicating a change in the 004 plane spacing consistent with strain relaxation. Importantly, the peak width and magnitude of the film is comparable before and after transfer, which suggests comparable crystal quality, at least in the aggregate.

A more complete picture of the crystal state before and after transfer is obtained by making a full reciprocal space map around the position of the diffraction peak of interest. By taking a series of scans in 2θ with varying $\theta/2\theta$ offset, a reciprocal space map can measure the in-plane and out-of-plane scattering vector of the film relative

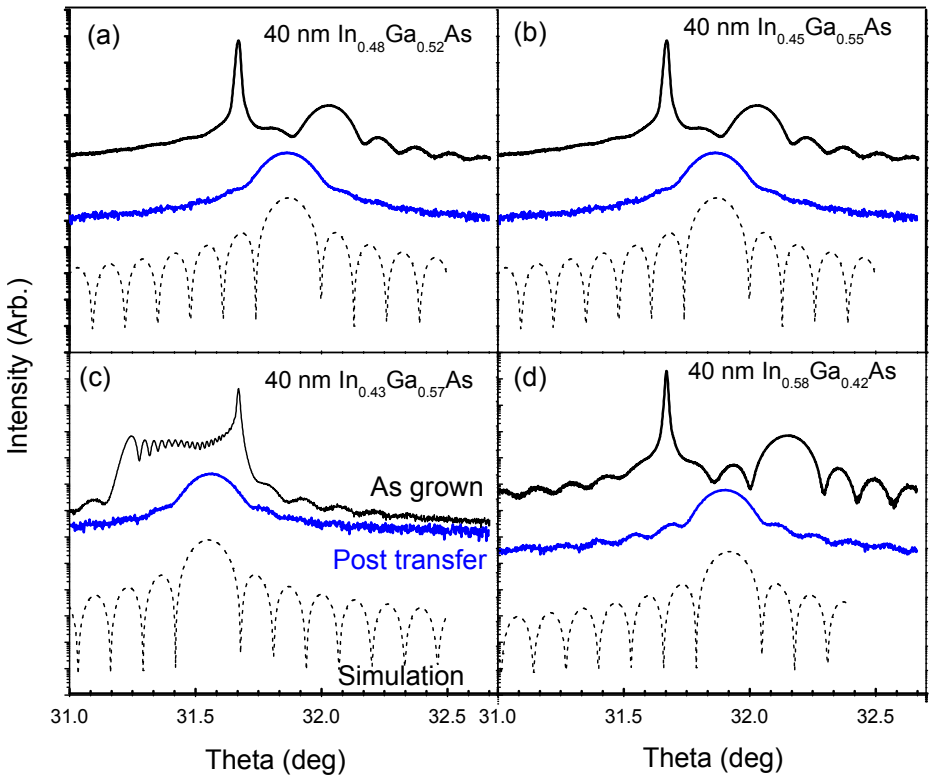

Figure 3.8. X-ray diffraction rocking curve measurement of the (004) reflection of InGaAs virtual substrate films before and after transfer to silicon. Post-transfer peak position shows complete strain relaxation and corresponds to simulated profile.

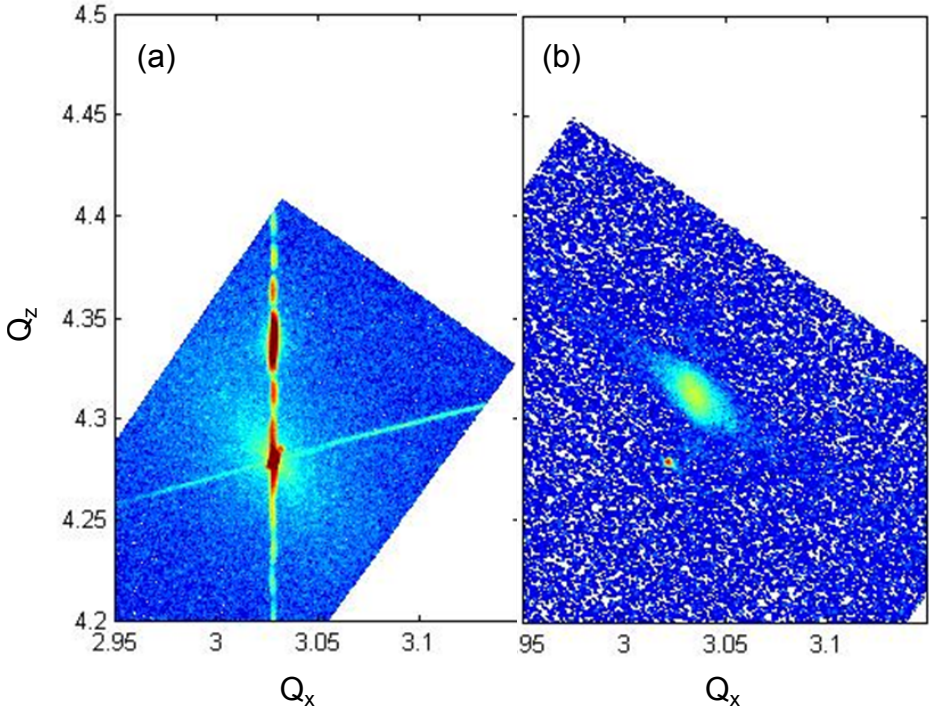

Figure 3.9. Reciprocal space map of the (224) peak for 5.83 A InGaAs virtual substrate film before (a) and after (b) transfer to the silicon handle wafer. The scattering vector change in panel (b) indicates full elastic strain relaxation.

to the substrate. Figure 3.9 shows the reciprocal space map for the 5.83 A InGaAs film (224) peak both before (a) and after (b) transfer to the silicon handle. As grown on the InP wafer, the film in-plane scattering vector Qx has the same value as the InP in-plane scattering vector. After transfer, both Qx and Qz shift to new values corresponding to full relaxation to a cubic structure.

3.4.4 Cracks

While the XRD measurements of many virtual substrate samples indicated high-quality, elastically relaxed films in the aggregate, all the post-transfer films exhibited an extensive network of cracks. These cracks penetrated through the film to the handle substrate and resulted in 1-5 micron gaps between the continuous areas of film. Figure 3.10 shows a selection of optical micrographs revealing the extent and

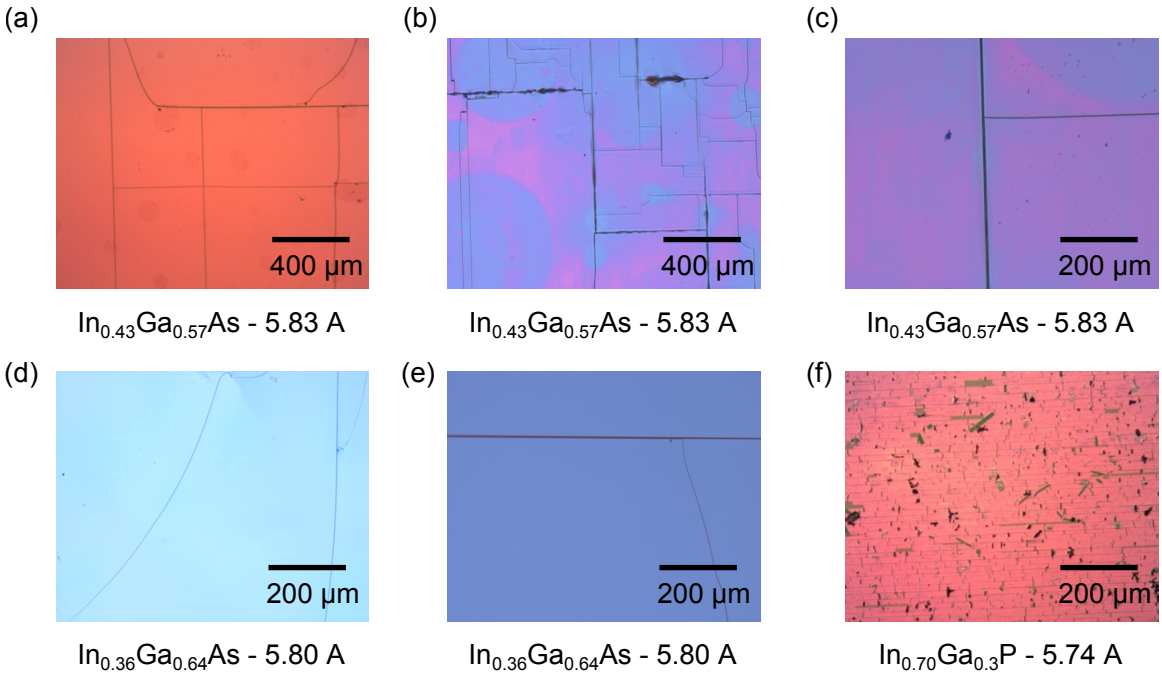

Figure 3.10. Optical microscope images of virtual substrate films as transferred to silicon. All films exhibit a network of cracks following the [110] cleavage direction.

nature of these crack networks on a variety of different samples. In most cases the transferred film had several uncracked areas 100 to 400 microns square, as well as regions with more closely spaced cracks. Almost all cracks were aligned with the 110 cleavage planes.

The crack network is evident as soon as the film is removed from the substrate etch while it is still on the wax handle. The crack spacing is not correlated with the amount of strain in the film as grown. Increasing the thickness of the film resulted in a much denser crack network.

The InGaP films were more severely cracked than the InGaAs films due to the architecture of the film structure in combination with the buried sacrificial etch. The buried AlAs etch layer was separated from the InGaP film by a 100 nm buffer of GaAs. The buffer was intended to protect the thin InGaP film from exposure to the HF acid etch used to remove the AlAs. While it did provide etch protection, the bilayer combination of buffer and InGaP film had a large strain differential between the two layers. Because the two materials have a similar modulus that is much greater

than that of the wax, the bilayer system tends to buckle until the internal forces are balanced. The wax cannot supply enough traction to constrain the film-buffer bilayer to a planar configuration. Both InGaP and GaAs are materials with low fracture toughness, and therefore the buckling pattern results in cracks.

The failure of the InGaP films suggests that local buckling may be a factor in the crack network development of the InGaAs films as well [45, 46]. As the last micron of InP is removed, it will also form a strained bilayer with the InGaAs. The non-planar nature of the InP etching will result in different regions of the film being vulnerable to buckling at different times and with different spatial period.

If buckling due to the wax handle being unable to restrain the strained film/thin substrate ensemble to a planar configuration is the root cause of the cracks in the relaxed film, then a transfer method that provides a more rigid out-of-plane restraint should be able to prevent cracks from forming. Using a layer of wax thinner than the amplitude of the likely buckling pattern is one possibility. Attempts to achieve this experimentally were not successful.

3.5 Growth on the virtual substrate

In order to serve as growth templates, the virtual substrates must be able to withstand temperature cycling up to 500 C without film delamination or damage. Heating experiments in a rapid thermal annealer (RTA) with ambient nitrogen flow indicated that the virtual substrate could withstand growth temperatures provided that the temperature was raised slowly to 500 C. A 20 minute ramp time was sufficient to allow volatile species trapped at the bond interface to escape slowly without causing blisters or local delaminations. The virtual substrate exhibited no visible changes after being heated to 500 C gradually over the course of 20 minutes. The substrate was held at 500 C for only 5 minutes to prevent loss of arsenic due to the lack of a group V reactant overpressure.

While all virtual substrates showed crack networks, the prevalence of uncracked areas hundreds of microns square was deemed sufficient to attempt growth on the

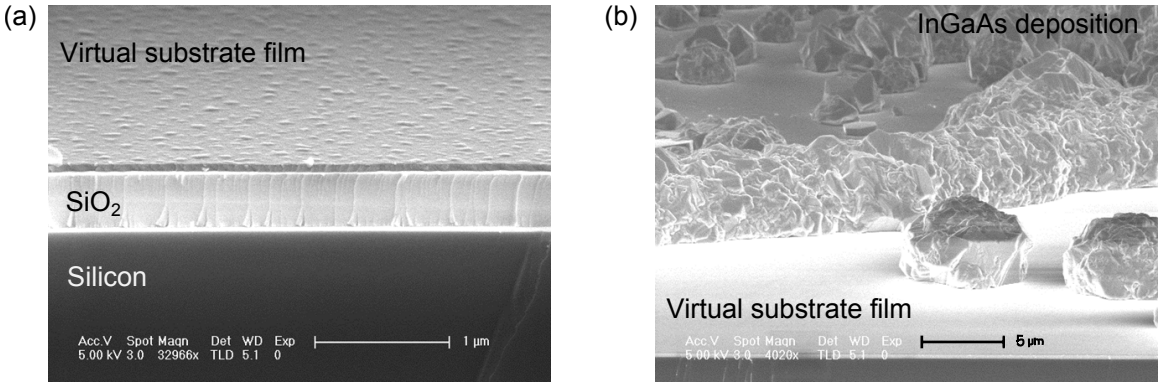

Figure 3.11. SEM images of first growth attempt on 5.83 A virtual substrate.

virtual substrate. A virtual substrate consisting of a 2 inch diameter InGaAs film with lattice parameter 5.83 Angstroms and 47% indium on a 4 inch diameter Si/SiO2 wafer was sent to Sumika, who attempted to grow a lattice-matched InAlAs/InGaAs double-heterostructure 200 nm thick.

Unfortunately, this growth attempt was not successful, as is evident from the SEM images in Figure 3.11. These micrographs show that growth failed to nucleate properly on the virtual substrate surface. The high magnification image in panel (a) shows the virtual substrate film still bonded to the SiO_2 layer on the silicon wafer. In the region where no material deposited onto the virtual substrate, there are small features which suggest possible surface contamination. It is also possible that a thin native oxide was present and inhibited epitaxial growth.

3.5.1 Surface preparation for virtual substrate

Further growth attempts on the virtual substrate required a method to identify and remove any surface oxide. X-ray photoelectron spectroscopy (XPS) measurements verified that the As 3d, In $3d_{5/2}$ and Ga $2p_{3/2}$ peaks had shoulders consistent with the presence of a mixed oxide at the surface [47, 48]. After a 30 second etch in 10% HF solution, the peak shapes return to the profile associated with a pristine surface, as shown in Figure 3.12. The brief etch does remove some of the thermal oxide from the silicon handle wafer, but it does not remove it completely, and the SiO_2 remaining

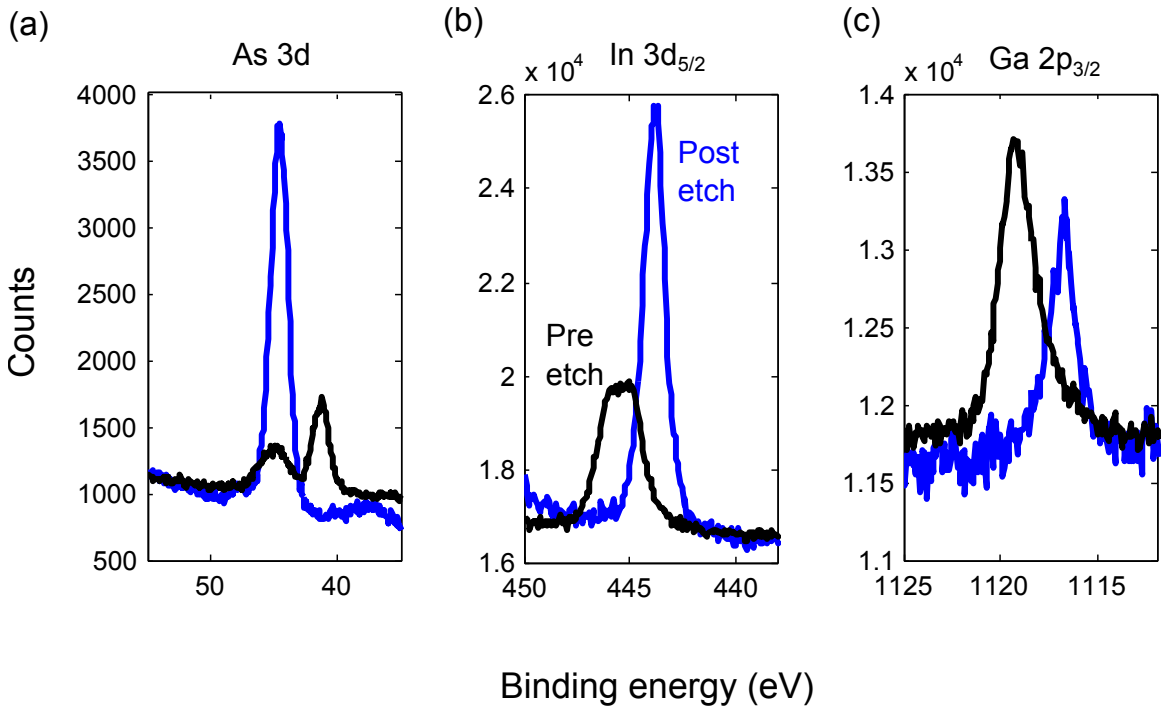

Figure 3.12. XPS measurements of the virtual substrate surface before and after a 30 second etch in 10% HF. The (a) As 3d, (b) In3d5/2 and (c) Ga2p3/2 peaks all show reduction of secondary peaks consistent with oxide removal.

is sufficient to prevent subsequent III-V growth on regions of the virtual substrate that are not covered by the InGaAs film.

Project collaborators at Boeing Spectrolab were instructed to perform a 30 second etch with 10% HF on the virtual substrates, followed by a deionized water rinse and nitrogen drying, immediately prior to placement in the MOCVD reactor for future growth attempts.

3.5.2 Solar cell structures grown on virtual substrates

The second round of growth experiments attempted to grow lattice-matched material on InGaAs virtual substrates with 5.80 and 5.83 Angstrom lattice constants. Spectrolab was supplied with multiple virtual substrates at each lattice constant, mostly consisting of 1/4 of a 2" wafer area transferred to a 2" Si/SiO2 handle. Spectrolab used a sub-set of the virtual substrates to calibrate composition and growth condi-

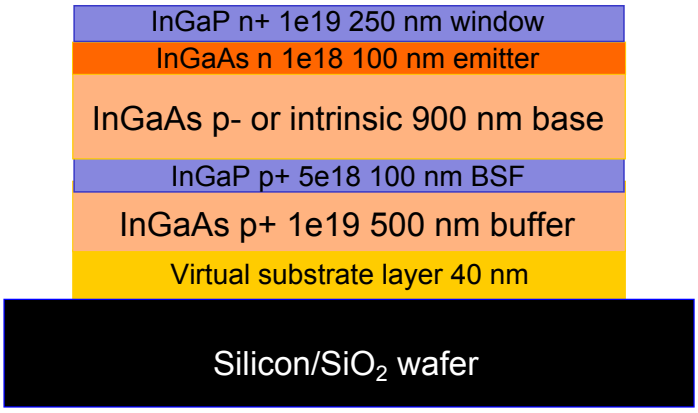

Figure 3.13. Schematic of layer thickness, composition and doping for solar cell structure grown on virtual substrate by Boeing Spectrolab.

tions for both the InGaAs absorber material and the InGaP window material. Finally, Spectrolab attempted to grow a single-junction solar cell lattice matched to the virtual substrates. The designed structure of the solar cell is shown schematically in Figure 3.13.

Figure 3.14 shows the virtual substrates used in the second-round growth attempt both before and after growth. The specific type of structure is listed with the images. The growth is visibly low-quality, and crack defects in the virtual substrate propagate into the structure on top. Figure 3.15 shows optical micrographs of the solar cell structures.

3.5.3 Crystal quality of growth

While the quality of the growth experiments was disappointing, xrd measurements verified that the material is mostly crystalline and lattice matched to the virtual substrate. Figure 3.16 shows the 224 reciprocal space map of the 5.83 solar cell growths and the virtual substrates on which they were grown, and Figure 3.17 shows these maps for the 5.80 A solar cell. In both cases the solar cell material peak is aligned with the virtual substrate peak. However, the growth peak is very broad, indicating the presence of dislocations and/or mis-oriented growth throughout the material. This is not surprising, given the visibly defective nature of the material.

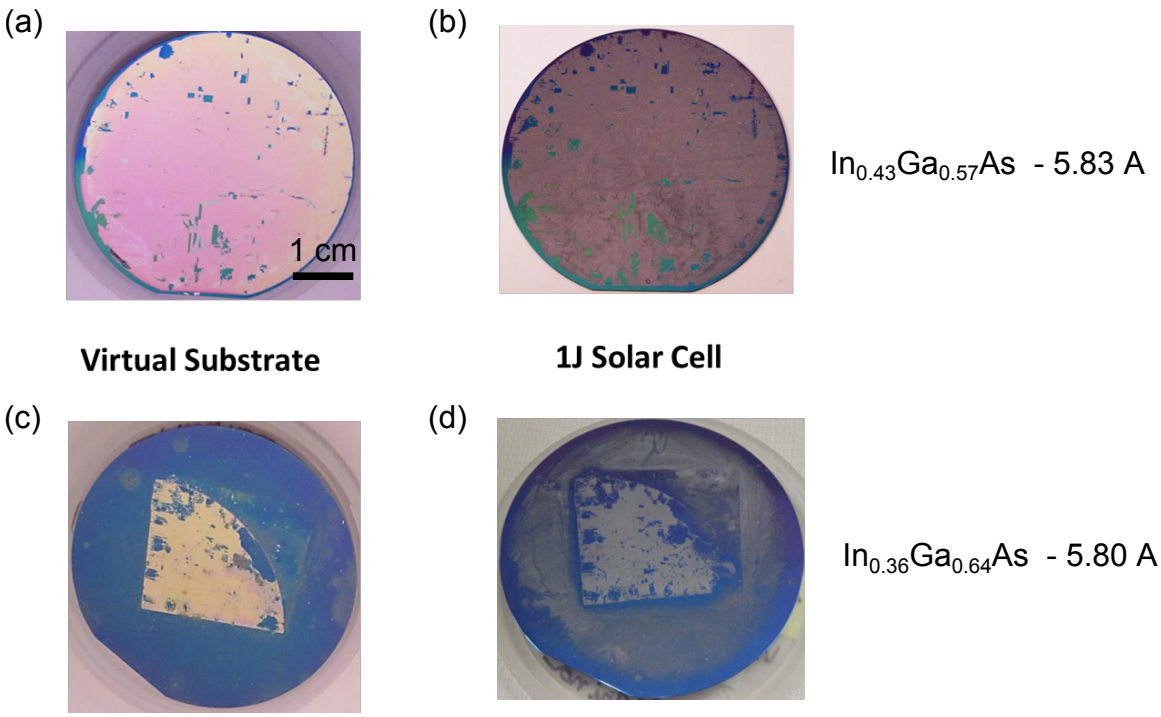

Figure 3.14. Photographs of virtual substrate templates before and after growth of solar cell structure.

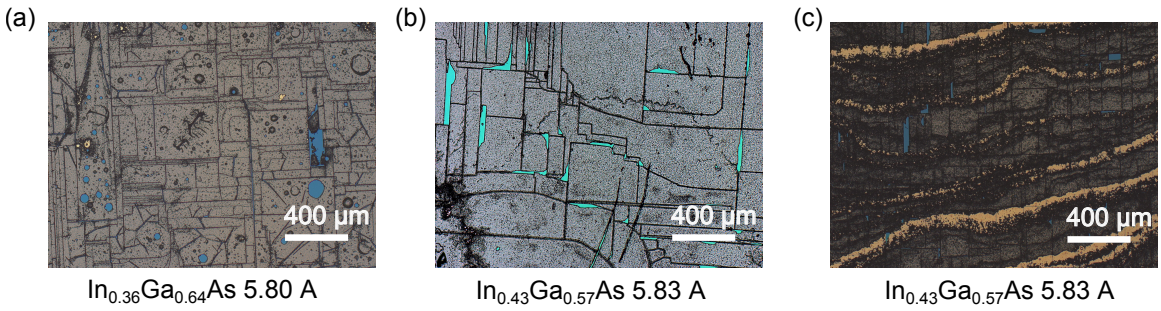

Figure 3.15. Optical microscope images of virtual substrate templates after growth of solar cell structure.

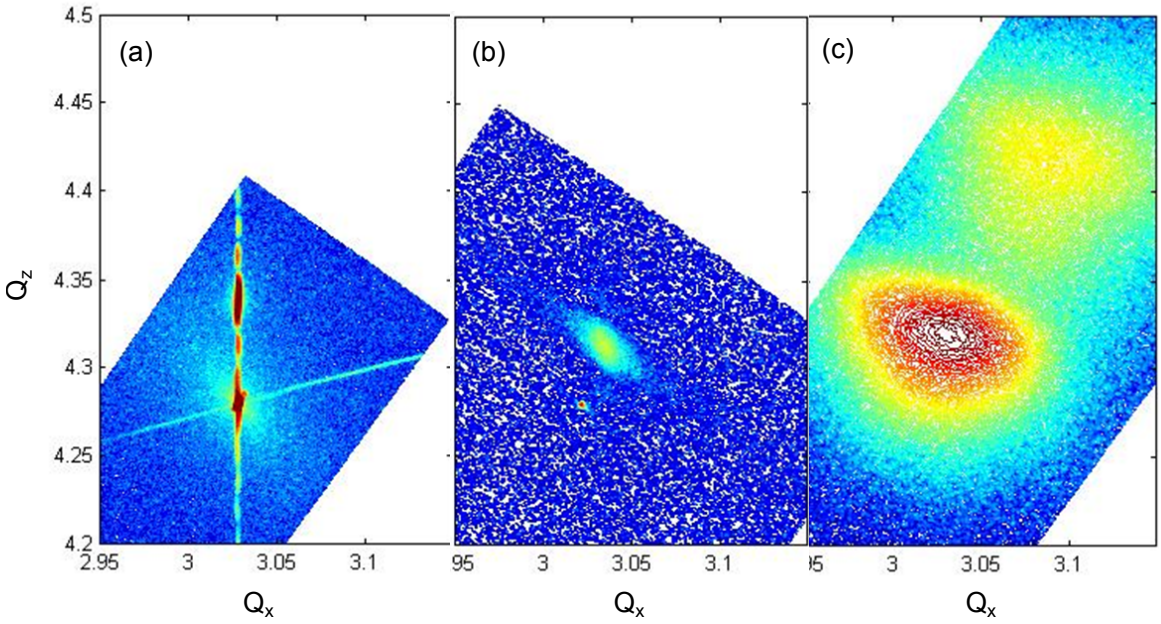

Figure 3.16. Reciprocal space map of 5.83 A virtual substrate template (a) as grown on InP, (b) after template fabrication, and (c) after solar cell growth attempt. The Qx and Qz scattering vector of the solar cell material match those of the relaxed template film. The broad peak suggests defective material.

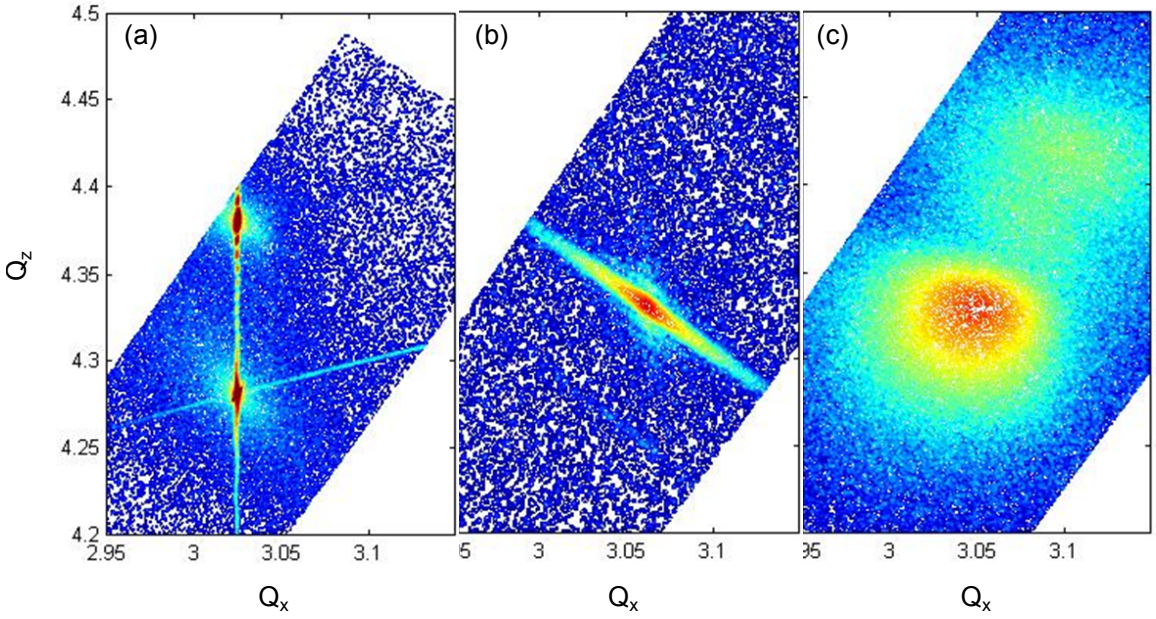

Figure 3.17. Reciprocal space map of 5.80 A virtual substrate template (a) as grown on InP, (b) after template fabrication, and (c) after solar cell growth attempt. The Qx and Qz scattering vector of the solar cell material match those of the relaxed template film. The broad peak suggests defective material.

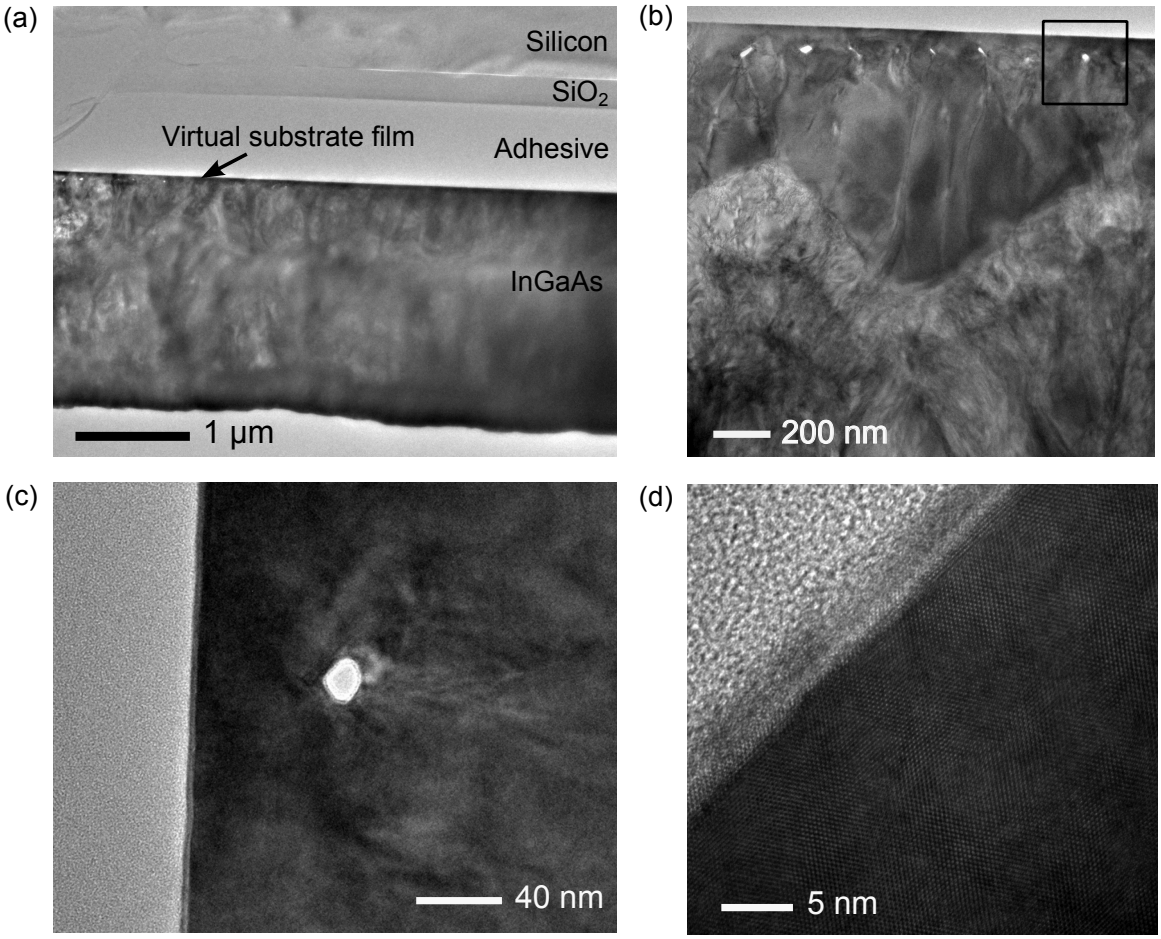

Figure 3.18. Cross sectional TEM measurement of 5.83 A InGaAs solar cell grown lattice matched to virtual substrate template.

Cross-section TEM measurements of the solar cell structure revealed a network of voids at the interface between the virtual substrate film and the growth material. Between these voids, the growth is epitaxial, and there is no visible differentiation between the template and growth material. However each void results in a high density dislocation network, and these networks coalesce as the material thickness increases. Figure 3.18 shows the TEM results. While all the TEM samples prepared had a gap between the virtual substrate film and the SiO_2 layer on the handle, the SEM images suggest this delamination occurred during sample preparation rather than during growth. Further study is needed to definitively verify that the virtual substrate film remains bonded to the handle during growth, however.

3.6 Conclusion

These experimental efforts establish the initial proof of concept for the virtual substrate template. Future work must determine the source of the pervasive crack network during fabrication and identify methods to prevent crack formation. Once crack-free templates can be fabricated consistently, the next step is to determine the source of the voids at the epitaxial growth front. Improved surface preparation and treatment to ensure complete removal of all trapped volatiles prior to growth are both good avenues of inquiry towards making the virtual substrate a truly functional epitaxial template. Finally, the virtual substrates fabricated thus far do not completely span the range of lattice constants between InP and GaAs. Dislocation nucleation was substantial in the as-grown films with more than 1.5% lattice mismatch. Exceeding this strain limit may require much thinner virtual substrate films, perhaps grown by MBE rather than MOCVD. Experiments testing the minimum required thickness for the virtual substrate to function as an epitaxial template will be useful in expanding the range of lattice constants the virtual substrate can supply.

Chapter 4

Optimizing ensembles for radiative coupling

As described in Chapter 1, all conventional solar cells emit light when operating at positive voltage [35].

While conventional diode-based solar cells inevitably emit light through radiative recombination at positive voltage, that emitted light need not necessarily be completely lost. A system with multiple sub-cells presents the opportunity for light emitted from one sub-cell to be absorbed by a different sub-cell of lower band gap, which will then recover some of the energy in those photons and convert it to electricity [20, 49]. The amount of energy recovery depends on the proportion of emitted photons that are re-absorbed and the band gap difference between the emitting and absorbing sub-cells.

Even systems with fractional transfer of emission can benefit from radiative coupling if the sub-cells have sufficient radiative efficiency. Taking full advantage of radiative coupling requires incorporating the phenomenon into the system design and optimization that includes the interaction of sub-cells. Most obviously, this means designing an optical system to facilitate radiative coupling. Beyond the optical design, this chapter explores the benefit of adjusting band gap combination and sub-cell operating point to maximize the benefit of radiative coupling and increase overall system efficiency.

4.1 What is the max power point?

Traditional treatment of radiative coupling between isolated cells assumes all cells operate at their individual max power point. The max power point is the voltage at which the maximum power is extracted from the device. It corresponds to the threshold at which increasing radiative emission outweighs the additional power gained by collecting current at a higher voltage [8]. Because the radiative emission from a cell is purely a function of its band gap and voltage, the max power point is affected only by the amount of light the cell absorbs (its short-circuit current).

If all sub-cells operate at their individual max power point, the amount of photons transferred between sub-cells is determined by each sub-cell's short circuit current, and the entire ensemble's performance is calculated sequentially.

4.1.1 Operating at higher voltage

The max power point determination assumes that all radiatively emitted photons are completely lost. A system with radiative coupling between sub-cells allows some portion of this emitted photon energy to be recovered, and this recovery raises the possibility that operating at a higher voltage might result in larger power collection overall.

A graphical interpretation of this phenomenon is presented in Figure ‘4.1.

Panel (a) shows the ideal J-V curve of a 1.42 eV solar cell. When the cell operates at its max power point voltage, the power converted corresponds to the area of the purple rectange. If all radiatively emitted photons are directed to a cell below operating at some particular voltage, some of the lost radiated power is recovered, corresponding to the green rectange. In panel (b) the 1.42 eV cell operates at a voltage higher than its V_{mpp} value, which causes the radiative losses to increase. Again, most of the radiative losses are converted in a second cell (shown by the green rectangle), and the yellow rectangle shows the extra radiative losses that are not recovered in the downstream cell. By operating at a higher voltage, the 1.42 eV cell is able to extract a bit more energy from the photons absorbed. This additional power corresponds to

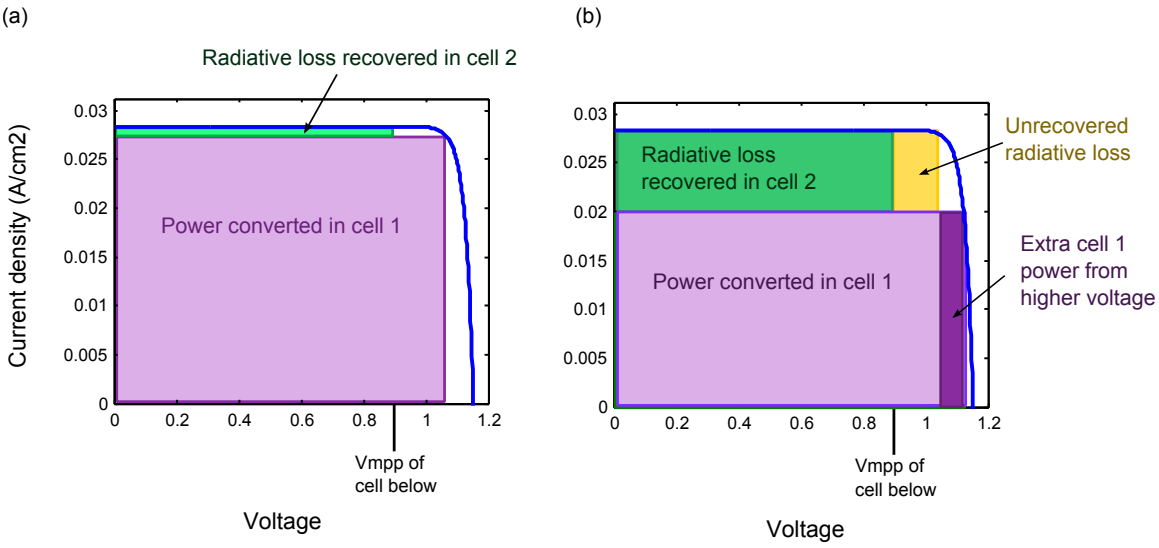

Figure 4.1. Schematic of system interaction changing the maximum power point voltage for the top cell due to radiative loss recovery in a lower band gap cell.

the dark purple box in panel (b). If the area of the dark purple box is greater than the yellow box, the system of the two cells will convert more power with the 1.42 eV cell operating at a voltage higher than its isolated maximum power point. This schematic illustrates the way system effects can combine to increase efficiency.

4.1.2 Voltage-enhanced radiative coupling in the two sub-cell case

To explore the potential benefit of voltage-enhanced radiative coupling and learn how much additional voltage might be beneficial, a simple test case consists of a system with two ideal sub-cells with perfect radiative coupling from the top cell to the bottom. Figure 4.2 maps the system efficiency as a function of top and bottom sub-cell band gap. For each combination of band gaps, the total efficiency was calculated, with the top cell operating at its individual maximum power point and at voltages from ten to fifty millivolts higher than Vmpp. The highest of these six efficiency values is mapped versus the sub-cell band gap values in panel (a). Panel(b) of Figure 4.2 shows the optimal top cell operating voltage relative to Vmpp for each band gap combination.

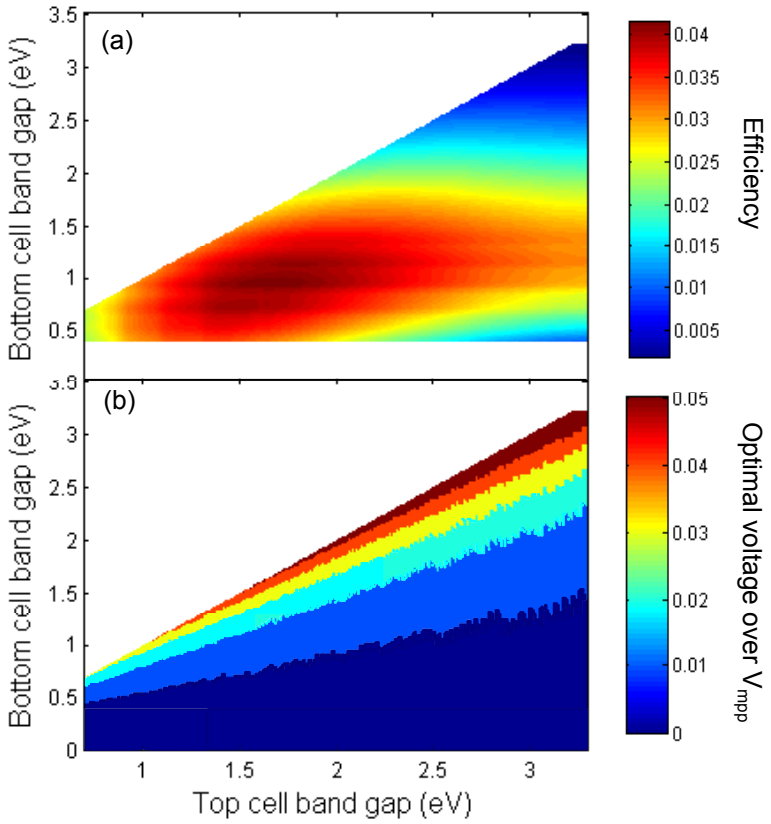

Figure 4.2. Radiative coupling in a system with two sub-cells. Panel (a) shows the efficiency versus top and middle cell band gap. Panel (b) shows the optimal top cell voltage relative to the isolated max power point voltage.

Unsurprisingly, the maximum efficiency point corresponds to a top cell band gap of 1.64 eV and a bottom cell of 0.94 eV. These are the optimal band gap values for a two-cell spectrum splitting ensemble with electrically independent sub-cells under the AM1.5D spectrum (at one sun). Interestingly, the peak efficiency value corresponds to a point where the top cell operates 10 mV above its Vmpp value. The efficiency of the system with the top cell operating at this higher voltage is 0.19% higher (relative) than when the top cell operates at Vmpp.

The relative benefit of voltage-enhanced radiative coupling is small for the optimal two sub-cell ensemble, because the need to match the solar spectrum results in a large difference in band gap between the two sub-cells. In turn, this means that a large percentage of the radiatively emitted photon energy is lost to thermalization after it is absorbed in the bottom sub-cell. Were the sub-cells more closely spaced in band gap value, as in a spectral splitting ensemble with more sub-cells, the optimal voltage would be higher. The diagonal cut-off line in Figure 4.2 corresponds to the case where the bottom cell is equal to the top cell in band gap. The optimal voltage values in panel b increase with proximity to that line, particularly as the top cell band gap decreases, because the percentage of emitted photon energy recovered in the bottom cell increases both as the top cell band gap (and emitted photon energy) decreases and as the separation between sub-cell band gap decreases. With a high percentage of emitted energy recovered, the benefit of collecting the top cell current at a higher voltage outweighs the loss of current due to enhanced radiative emission.

Figure 4.3 maps the relative efficiency benefit of operating the top cell at a higher voltage relative to Vmpp versus the top and bottom cell band gap for the two-cell case. At the optimal band gap combination, the relative benefit is very slight at 0.19%, but the benefit increases to a 4% improvement in the region near the cut-off line. This improvement is relative to ideal radiative coupling with the top cell operating at Vmpp. This trend indicates that voltage-enhanced radiative coupling is a strategy worth pursuing in ensembles with closely-spaced band gap values, particularly in the higher band gap sub-cells.

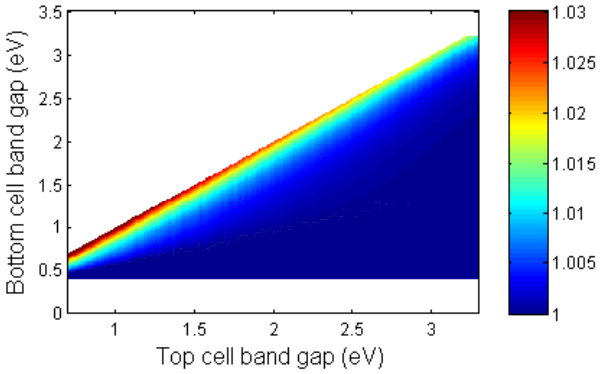

Figure 4.3. Performance improvement from voltage-enhanced radiative coupling relative to radiative coupling with the top cell operating at its isolated Vmpp.

4.2 Practical approaches to radiative coupling design

The analysis in section 4.1.2 assumes both ideal sub-cells and complete transfer of photons emitted by the top cell to the bottom cell. Achieving this perfect transfer requires some optical device that is non-reciprocal in its behavior, because the top cell must be able to absorb all incident light with energy greater than or equal to its band gap value, yet none of its emission is allowed to radiate back in the direction of the sun [6, 20]. While some non-reciprocal optical structures have been experimentally realized, none are practically capable of providing one-way transmission for unpolarized light. In the absence of a practical non-reciprocal structure, realistic radiative coupling designs will inevitably have only partial transmission of radiatively emitted photons to down-stream sub-cells.

The percentage of emission transmitted to the lower sub-cells depends on the optical integration of the system. Various integration schemes are depicted schematically in Figure 4.1. If the cells are physically isolated, as in panel (a), negligible transmis-

sion will occur. Ensembles with sub-cells that are vertically stacked but separated by a medium with a refractive index different than the cell material, as shown in panel (b), will send approximately half of radiative emission to the correct sub-cell. Finally, ensembles where the cells are monolithically integrated, as in panel (c), can potentially result in most radiative emission being directed to the desired downstream sub-cell. As discussed in Chapter 1, the radiative emission of a solar cell is affected by the cell's optical environment. When the cell is placed on a substrate with a refractive index similar to the cell's, light emitted internally in the direction of the substrate can pass directly out of the cell without reflection. In contrast, internally emitted light directed towards the top of the cell will not escape the cell unless it is inside the escape cone determined by the refractive index of air and the cell's refractive index. All the sub-cells in a monolithic stack typically have very similar refractive index values, which conveniently allows high transmission of light through the device. Because sub-cells are substantially transparent to light emitted by sub-cells with lower band gap, in practice all sub-cells can be treated as having the same optical environment: with air on top, and an index-matched substrate below. In this configuration, with an index of refraction of 1 for air and 3.6 for the semiconductor 93% of light escaping a cell will be transmitted to the sub-cell below it.

4.2.1 Radiative coupling in series-connected ensembles

Monolithically integrated spectrum splitting ensembles typically require the sub-cells to be wired in electrical series due to the practical challenge of contacting the sub-cells independently. Designing series-connected ensembles for radiative coupling presents a particular challenge, because the series connection forces all sub-cells to pass the same amount of current. In operation, when a sub-cell is forced to operate at a lower current than its Jmpp, the sub-cell voltage increases, thereby increasing its radiative emission and lowering its current to the constrained level. That excess radiative emission could conceivably be directed to the sub-cell that was restricting the ensemble current, creating a complicated feedback in the ensemble behavior.

The interaction between radiative coupling and current matching in series-connected

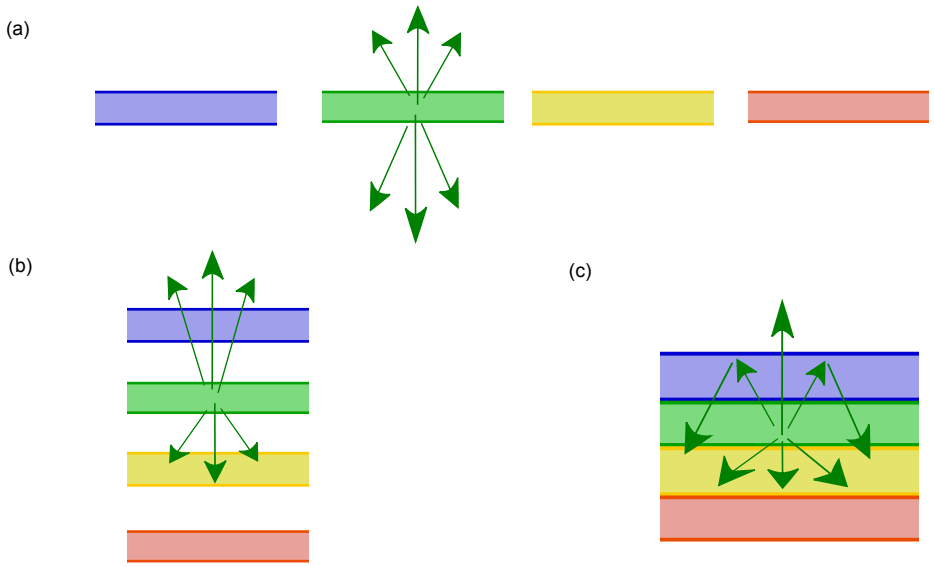

Figure 4.4. Schematic of spectrum splitting sub-cell configurations and the potential for radiative coupling between sub-cells. The monolithic stack directs a high percentage of a sub-cell's radiatively emitted photons to the sub-cell below, where they can be absorbed.

ensembles can be accounted for by the following procedure. First, consider the top two sub-cells of the ensemble. Each has a J-V relationship determined by the detailed balance equation. The series-connection constrains the sub-cells to operate at the same current density, resulting in equations 4.1 - 4.3 .

$$J_1(V_1) = J_{abs_1} - J_{rad_{1up}}(V_1) - J_{rad_{1down}}(V_1) \tag{4.1}$$

$$J_2(V_2, V_1) = J_{abs_2} - J_{rad_{2up}}(V_2) - J_{rad_{2down}}(V_2) + J_{rad_{1down}}(V_1) \tag{4.2}$$

$$J_{abs_1} - J_{rad_{1up}}(V_1) - J_{rad_{1down}}(V_1) = J_{abs_2} - J_{rad_{2up}}(V_2) - J_{rad_{2down}}(V_2) + J_{rad_{1down}}(V_1) \tag{4.3}$$

Note that radiative coupling results in the current for sub-cell 2 containing a term dependent on sub-cell 1's voltage, $J_{raddown1}(V_1)$. To identify the values of V_1 and V_2 that correspond to J_1 and J_2 being equal, subtract $J_{raddown1}(V_1)$ from both sides of

equation 4.3 to get equation 4.4. This equation now gives a new pair of matched J-V relationships that can be solved numerically for V_1 and V_2 over a range of current values.

$$J_{abs_1} - J_{rad_{1up}}(V_1) - 2J_{rad_{1down}}(V_1) = J_{abs_2} - J_{rad_{2up}}(V_2) - J_{rad_{2down}}(V_2) \tag{4.4}$$

Finally, $J_{raddown1}(V_1)$ is added back to both new J-V relationships. Performing this current-matching operation for each pair of sub-cells sequentially from highest to lowest gives a current matching J-V relation for each sub-cell, and these collectively give the J-V relationship for the entire ensemble.

Accounting for radiative coupling in series-connected ensembles can drastically change the projected performance of some band gap combinations. Figure 4.5 shows the simulated J-V behavior of three different triple junction series-connected ensembles. The first design has band gaps that are current-matched under AM1.5D. The second is the lattice-matched Ge/GaAs/InGaP design, and the third design has band gaps chosen to be deliberately not current matched under AM1.5D. The ensemble band gaps and efficiencies without radiative coupling are shown in table 4.2.1. In all cases the red, blue and black lines correspond to the individual sub-cell J-V curves with (solid) and without (dotted) radiative coupling. The black dashed curves correspond to the ensemble J-V relation with radiative coupling.

The effect of radiative coupling on these designs is radically different. The current-matched ensemble has an efficiency of 47.32% without and 49.22% with radiative coupling (one sun). The lattice-matched design efficiencies are 42.45% and 44.49%, respectively. This design gets much less benefit from radiative coupling, because its total current is limited by its top and middle sub-cells. In both cases the efficiency increase comes from a slight increase in the middle and bottom sub-cell operating point. By contrast, the third design has an efficiency of 37.74% without and 46.72% with radiative coupling. The design is severely current-limited by its middle sub-cell without radiative coupling but nicely current matched with it, and consequently it has

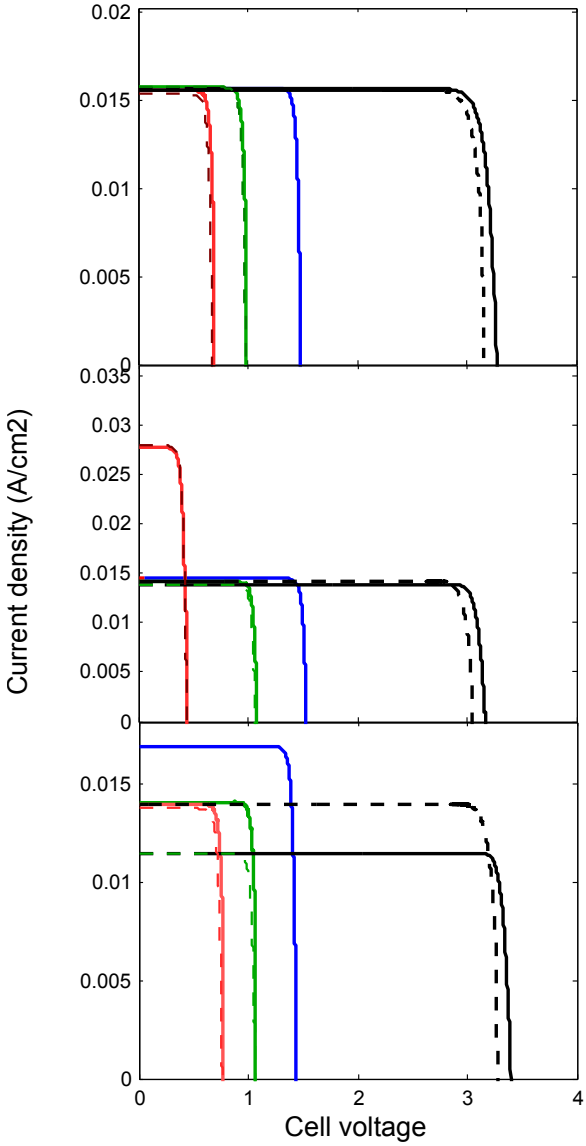

Figure 4.5. Series-connected performance of candidate ideal triple junction ensembles with and without radiative coupling between subcells. Panel (2) shows the ensemble with optimal current matching under AM1.5D. Panel (b) shows the commercially available lattice-matched Ge/GaAs/InGaP design. Panel (c) shows a 1.03/1.42/1.8 eV design.

Top Eg	Middle Eg	Bottom Eg	Efficiency with no coupling	Efficiency with coupling
1.84	1.33	0.93	47.32%	49.22%
1.9	1.42	0.67	42.45%	44.49%
1.8	1.42	1.03	37.74%	46.72%

Table 4.1. Band gap values and efficiency for three series-connected triple junction shown in figure 4.5 both with and without radiative coupling between sub-cells.

a higher efficiency than the lattice-matched design once radiative coupling is taken into account. While the current-matched design still outperforms design 3, a designer does not always have complete freedom in choosing the band gaps of monolithically integrated sub-cells. The high efficiency of design 3's very counter-intuitive band gap combination indicates that some designs that were previously dismissed as inefficient may deserve new consideration.

4.2.2 Optimizing series-connected ensembles for radiative coupling

Optimizing series-connected spectrum splitting ensembles to account for radiative coupling presents many of the same challenges as optimizing the electrically independent ensembles in Chapter 2. While the ensembles will ideally be current-matched with the radiative coupling included, there is no simple way to predict which band gap combinations will meet this requirement. Fortunately, the simulated annealing approach described in Chapter 2 is easily applied to the task. Rather than start with a randomly-generated initial design, the optimization was seeded with the optimized series-connected ensemble from Chapter 2. The optimization again included two rounds, first with a widely-varying fluctuation applied to the ensemble and then with a narrow fluctuation. Each candidate design was evaluated for series-connected performance with radiative coupling, where 93% of each sub-cell's total emission was assumed to be absorbed in the subsequent sub-cell. The radiative emission was calculated based on an air interface at the top of each sub-cell and an index-matched

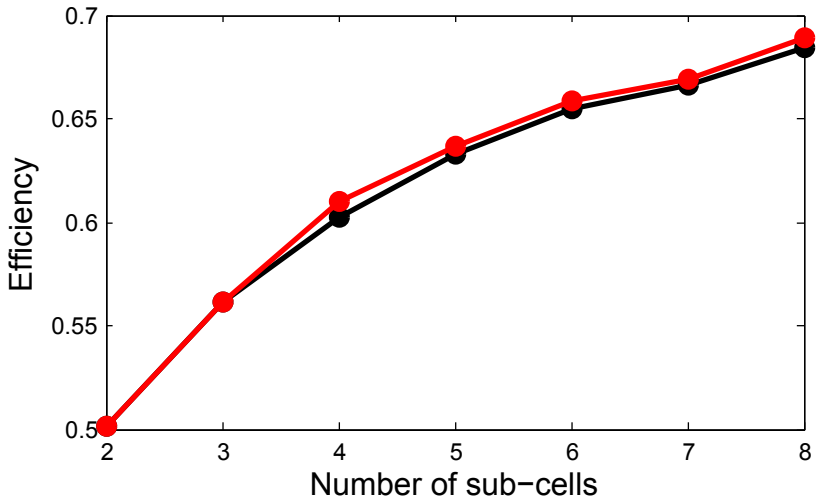

Figure 4.6. Efficiency of ideal series-connected ensembles with radiative coupling. Points in black correspond to ensembles optimized to be current-matched under AM1.5D, with radiative coupling neglected. Points in red correspond to ensembles optimized for maximum efficiency with radiative coupling.

interface at the bottom, with all cells having an index of 3.6.

Figure 4.6 shows the efficiency of series-connected ensembles with radiative coupling with 2 to 8 sub-cell. The black curve shows the efficiency of designs optimized such that each sub-cell absorbs an equal number of photons under AM1.5D. These are the same ensembles discussed in Chapter 2. The red curve shows the efficiency of ensembles with band gaps optimized to take advantage of radiative coupling. The plot shows a significant performance advantage for designs optimized with radiative coupling in mind. The benefit increases with increasing sub-cell number, which is consistent with the trend shown in Figure 4.3 of increased benefit as sub-cell spacing decreases. The lower level of improvement for the 7 sub-cell ensemble likely comes from the increasing sensitivity of these ensembles to current starvation when one sub-cell is under-illuminated. The optimization was not able to select repeated optimum values for these ensembles, and so a higher efficiency may be attainable. However, the performance of these designs is very sensitive to slight variations in band gap value, and consequently the optimum design may require an impractical level of control over sub-cell band gap (in the proxy of material composition) for experimental realization.

4.3 Conclusion

The examination of ensemble effects resulting from radiative coupling, while not complete, suggests additional efficiency benefits are achievable by accounting for this phenomenon in the design process. Future work should focus on adapting these results to account for realistic material quality, ptimizing electrically independent ensembles with sub-cells operating above their isolated max power point voltage, and the performance of other optical systems to determine how robust the effect is in other settings.

Chapter 5

Annual energy production of spectral splitting ensembles

The efficiency of photovoltaic systems is evaluated under standardized test conditions, which include the spectral composition and intensity of illumination [22, 23]. While standardization allows a fair basis for comparison of systems, performance in the installation environment must be extrapolated based on expected differences in temperature and illumination [21]. A variety of models attempt to predict energy production performance based on system efficiency and site-specific conditions, but these models typically restrict the variation in illumination to changes in intensity (total irradiance) and neglect spectral variation under the assumption that the efficiency of the photovoltaic system is not sensitive to the spectral composition of illumination. This chapter examines that assumption for the spectral splitting designs discussed in Chapter 2.

While it is simple to evaluate photovoltaic systems' efficiency under standard conditions, a truly efficient system will be able to convert a substantial portion of incident light into electricity regardless of the specific irradiance conditions. Solar power already suffers from the intermittent (though predictable) nature of sunlight and the corresponding low capacity factor relative to other electricity generation technologies. Therefore it is important to design for high performance under a variety of conditions.

Here, a year's worth of sunny day spectra were generated for a particular location to provide an estimate of the degree of spectral variation a system might experience over the course of a year. Using these spectra as the input for a detailed balance

calculation for different spectrum splitting ensembles resulted in a prediction of the relative cumulative performance of different designs.

5.1 Variability of incident solar illumination

The spectrum of sunlight incident on the earth's surface varies due to three main factors. The first is variation in the spectrum emitted by the sun. This source of variation is small, and accounts for no more than 0.3% of the photon flux variation at any wavelength [24]. The rest of this analysis therefor neglects accounting for variation in the spectrum incident at the top of the earth's atmosphere. The second source of variation is the path length of light through the atmosphere to the earth's surface [26]. This path length is typically reported in units of "air mass" where an air mass of 1 (AM1) corresponds to the depth of the atmosphere at the equator. As light passes through the atmosphere, some photons are absorbed or scattered by gases and suspended particles. The amount of attenuation at any particular wavelength is strongly dependent on the path length, which is in turn dependent on location and time of day and year. The final significant source of spectral variation is the specific composition of the atmosphere along the light path. The atmosphere has substantial variation in the local concentration of trace gases such as CO_2, ozone, water vapor, and other pollutants, as well as variation in the amount and type of particulate matter suspended in the air. All of these materials have specific absorption and scattering properties which affect the transmission of light at different wavelengths [25].

The effect of atmospheric composition and air mass on the incident spectrum can be simulated using a multiple scattering and absorption model, SMARTS, which is available from the National Renewable Energy Lab [50]. This model allows the user to specify a wide variety of atmospheric conditions as well as location and time. The user can simulate a variety of spectra, including the direct and diffuse components. This analysis chose Phoenix, Az as a location, because it is a city with a large direct component of the total irradiance. Because the designs capable of ultra-high efficiency identified in Chapter 2 all had moderate to high concentration, the analysis used only

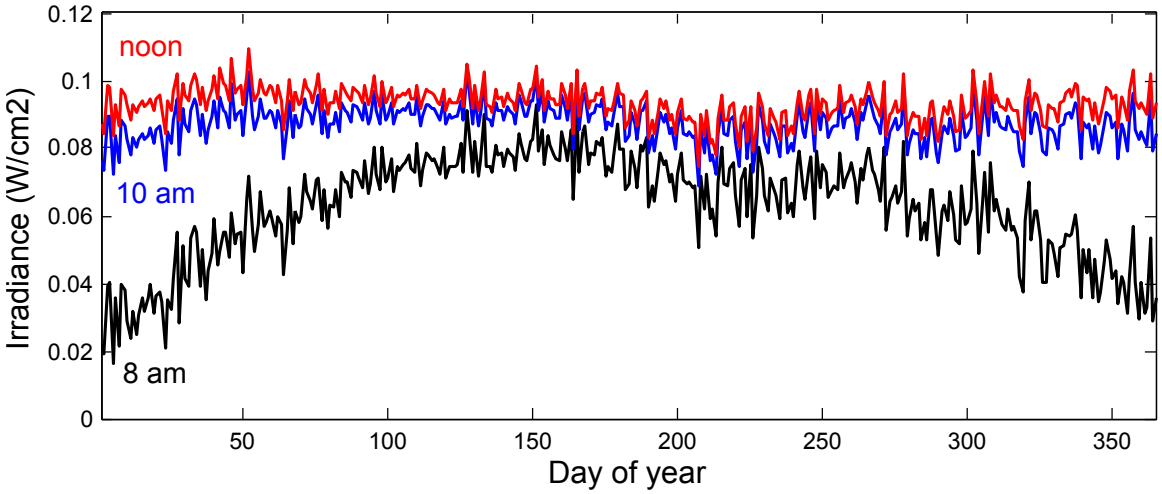

Figure 5.1. Irradiance at 8 am, 10 am, and noon versus day of year, as simulated for Phoenix, Az, using the SMARTS multiple scattering and absorption model and average atmospheric conditions.

the direct component of the irradiance. The acceptance angle of concentrating optics excludes most diffuse illumination from reaching the solar cell.

For each day of the year we generated spectra hourly from 8 am to 5 pm. Atmospheric conditions were taken from NOAA data for hourly normal values of temperature, pressure and dew point. These values are averages of measurements recorded from 1980 to 2010. Aerosol optical depth and precipitable water were generated daily from monthly mean and standard deviation values taken from the AERONET data set [51]. Atmospheric CO_2 concentration was set to 370 ppm and ozone concentration set to the standard in the SMARTS model. Figure 5.1 shows the total irradiance for each hour from 8 am, 10 am and noon over the course of the year. There is a wide range of values for each time of day, with a seasonal trend towards increased irradiance in the summer, as expected. The larger degree of variation for the 8 am curve is a result of the larger air mass at this time of day increasing sensitivity to atmospheric composition.

5.2 Spectrum splitting performance under varying illumination

Each of the 3650 spectra generated was used as the input spectrum for a detailed balance calculation of energy production for the spectrum splitting ensembles under consideration. In all cases the cells were treated as ideal, with unity absorption of photons designated for each sub-cell and purely radiative recombination. All calculations were performed at 500 suns concentration, and the captured power for each ensemble multiplied by one hour, thereby obtaining an average energy production for each active hour of the year per square centimeter of cell area.

The results of this calculation are shown in Figure 5.2. Panel (a) shows the efficiency of electrically independent, "independent" and electrically series-connected, "series" ensembles under the AM1.5D spectrum at 500 suns concentration. Panel b shows the projected annual energy production for independent and series ensembles based on the spectra generated for Phoenix. In all cases the series ensembles generate substantially less energy over the year than the corresponding independent ensemble with the same number of cells. The energy production difference ranges from 10% for the ensembles with 2 sub-cells to 25% for the ensembles with 20 sub-cells. The amount of energy produced increases with number of sub-cells for the independent ensembles, in contrast to the series ensembles. The energy production of these series-connected ensembles saturates with 10 cells and performance degrades slightly as additional sub-cells are added, despite the improvement in design efficiency. Clearly the performance of a series-connected spectral splitting ensemble under the standard AM1.5D spectrum is not an accurate prediction of its energy production capabilities under varying spectra.

5.3 How spectral variation affects efficiency

The large deficit in energy production for the series ensembles comes from spectral mismatch between the ensembles and the different realistic spectra. Spectral mis-

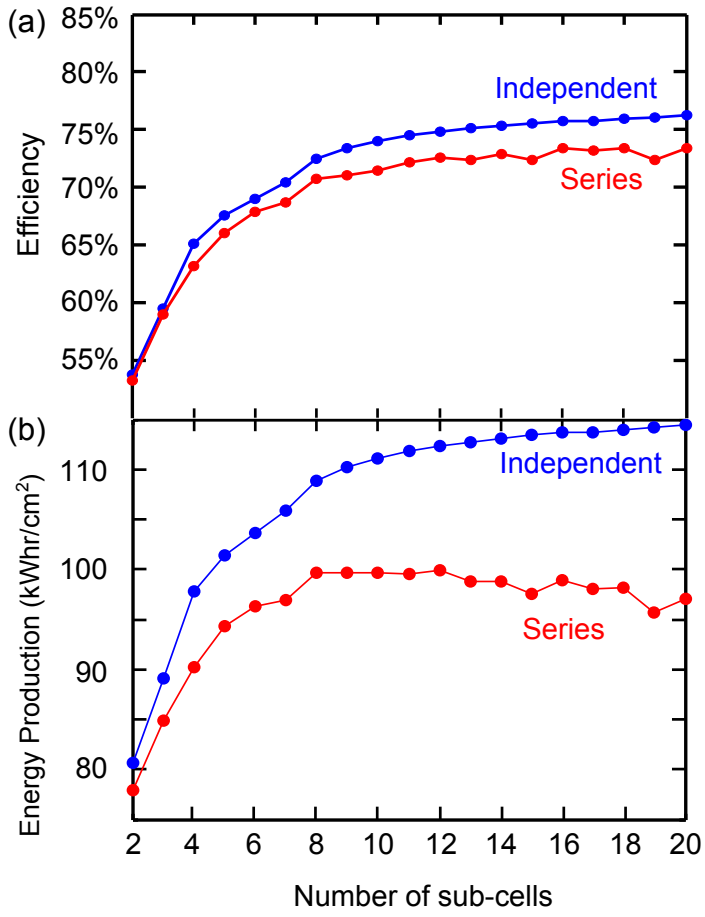

Figure 5.2. Detailed balance efficiency and simulated annual energy production for ideal series-connected and independent spectrum splitting ensembles operating at 500 suns.

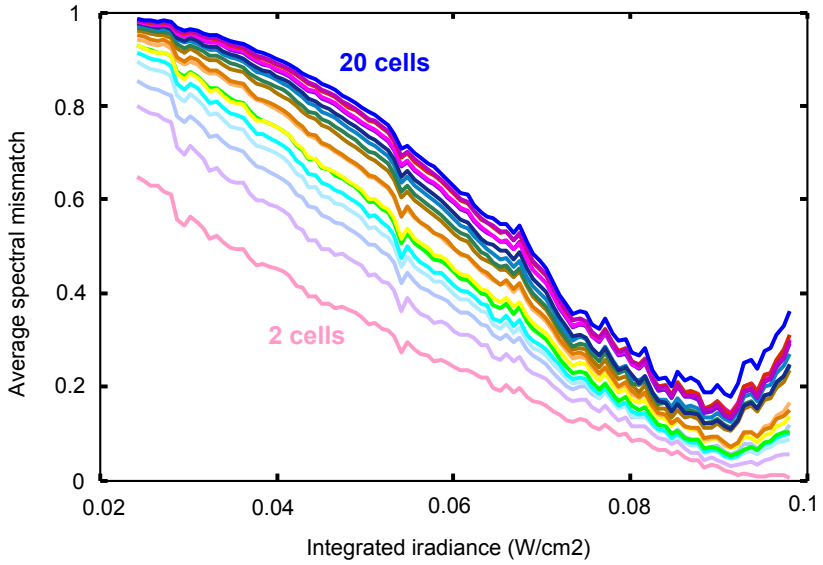

Figure 5.3. Spectral mismatch for series-connected ensembles. All incident spectra were sorted into 100 bins according to total irradiance, and spectral mismatch for the ensembles averaged over all spectra in each bin.

match is defined as 1 minus the ratio of the smallest sub-cell flux to the largest sub-cell flux. An ensemble with perfect current matching across all sub-cells will have a spectral mismatch of zero, while an ensemble with one sub-cell completely starved for current will have a mismatch of 1. Figure 5.3 shows the spectral mismatch of the series ensembles relative to irradiance level. The incident spectra are separated into one hundred power bins and the spectral mismatch for each ensemble averaged over the spectra in each bin. This plot shows a minimum spectral mismatch for all series ensembles at power levels of 900 to 950 W/m2, which is comparable to the 900 W/m2 of the AM1.5D standard. All series ensembles have increasing mismatch as the irradiance deviates from that level. Further, no ensemble has an average mismatch of zero at any power level. All ensembles are losing conversion efficiency due to the series connection constraint. Finally, at every power level, the average mismatch increases with the number of sub-cells.

There are two possible mechanisms that can cause spectral mismatch. In the first mechanism, the incident spectrum is close to the AM1.5D spectrum, but it includes extra photons in the sub-band for one or more sub-cells. The series electrical con-

nection will not allow the ensemble to collect the extra current absorbed in these sub-cells and the extra power is simply re-emitted radiatively, while the total ensemble produces as much power as it would under the AM1.5D spectrum. The second mechanism occurs when one or more sub-cells of the series-connected ensemble is starved of photons due to increased atmospheric absorption or scattering relative to AM1.5D. If one or more sub-cells is converting many fewer photons than it is allotted under the design spectrum, the series electrical connection will constrain the entire ensemble to this reduced current level. The current reduction will tend to create a large reduction in power conversion even when the incident power is close to the 900 W/m2 of the AM1.5D spectrum. Identifying the dominant cause of the efficiency deficit may suggest design alterations that can improve the relative performance of the series connected ensembles.

The independent ensembles were also designed for optimal performance under the specific AM1.5D spectrum, and therefore are likely to suffer a decrease in spectral efficiency under different illumination conditions. However, the penalty due to lower spectral efficiency is much lower than the penalty due to spectral mismatch experienced by the series ensembles. Figure 5.4 shows the average efficiency of the series and independent ensembles relative to irradiance level for different numbers of sub-cells. The ensembles with electrically-independent sub-cells, shown in panel (a), have average efficiencies that vary 5 to 6 absolute percent over the different irradiance levels, and efficiency increases with additional sub-cells at all irradiance levels. The far right section of panel (a) shows the efficiency of these ensembles under the AM1.5D spectrum. The design efficiency value for these ensembles is very close to the average efficiency over incident powers ranging from 500 to 1000 W/m2. This plot indicates that the instantaneous efficiency of electrically independent ensembles in the field under direct sunlight is likely to be very close to the design efficiency under AM1.5D throughout the year.

In contrast, the series ensembles, shown in Figure 2 panel (b) have efficiencies that vary by a minimum of 13 percentage points for the ensemble with 2 sub-cells. Ensembles with more sub-cells have an even larger range of efficiencies. The series

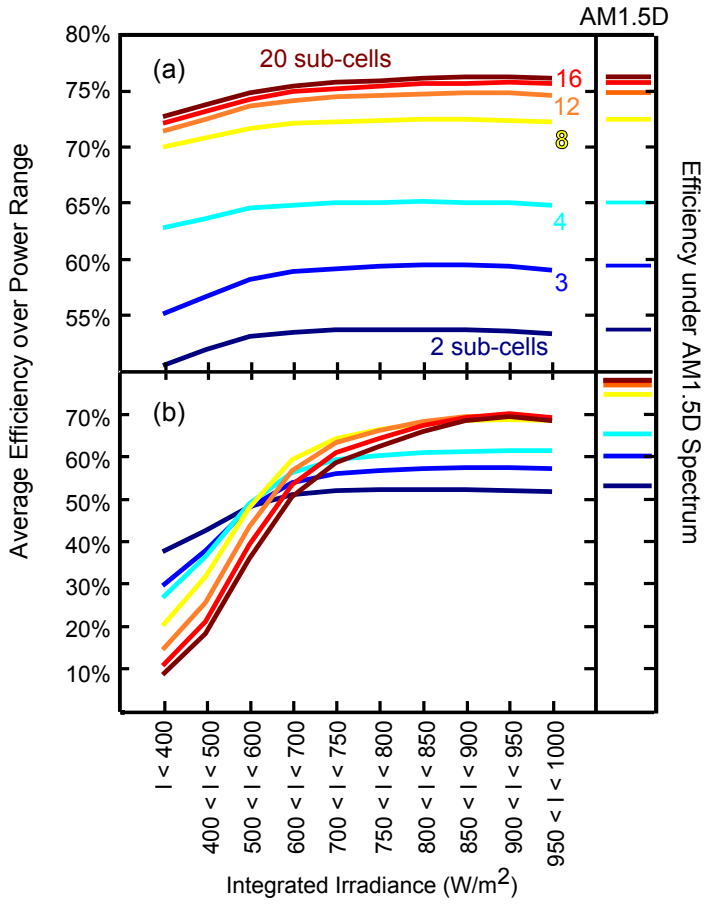

Figure 5.4. Average efficiency of (a) independent and (b) series spectral splitting ensembles under simulated incident spectra (at 500 suns). Performance is averaged over all spectra in the power categories listed on the x axis. Inset panels to the right show ensemble design efficiency under AM1.5D spectrum.

ensembles have their highest average efficiency under spectra in the 850 to 900 W/m2 irradiance level, and their efficiency drops off steeply at lower incident irradiance levels. Interestingly this efficiency drop-off is steeper as more sub-cells are included in the ensemble, so that at very low irradiance levels the efficiency decreases with additional sub-cells. The highest average efficiency for series-connected ensembles is achieved not by the 20 cell ensemble, but by the 16 cell ensemble. Again, the far right panel shows the ensemble efficiencies under AM1.5D illumination, and all design efficiencies are higher than the average ensemble performance at any irradiance level. The deficit between design and peak efficiency is only 0.8% absolute for the 2 cell ensemble, but it increases to 10% absolute for the 20 cell ensemble, indicating that the average field performance for series-connected ensembles with large numbers of cells will not be predicted well by the performance under the standard spectrum.

5.4 Impact on annual energy production

The effect of the power-dependent efficiency of the series-connected ensembles on annual energy production is illustrated by Figure 5.5. Panel a contains a plot showing the excess energy independent ensembles produce relative to the series ensembles with the same number of cells totaled over the power bins in panel shown in panel b. The electrically-independent ensembles have a substantial efficiency advantage in the lower power bins, resulting in a cumulative excess energy production of one quarter to one third of the excess in the high power bins, despite there being many fewer individual spectra and much less incident power in those bins. In particular, the bin for 600 to 700 W/m2 holds almost the same excess energy generation as the bin for 800 to 850 W/m2, despite the higher power bin representing more than twice that amount of total incident energy. More broadly, 75.6% of the annual incident energy is contributed by spectra with more than 800W/m2, yet 41% of the excess energy production by independent ensembles comes from converting the spectra with less than 800 W/m2, which is mostly due to the series-connected ensembles having very low efficiency for these spectra. This low-power conversion performance constitutes

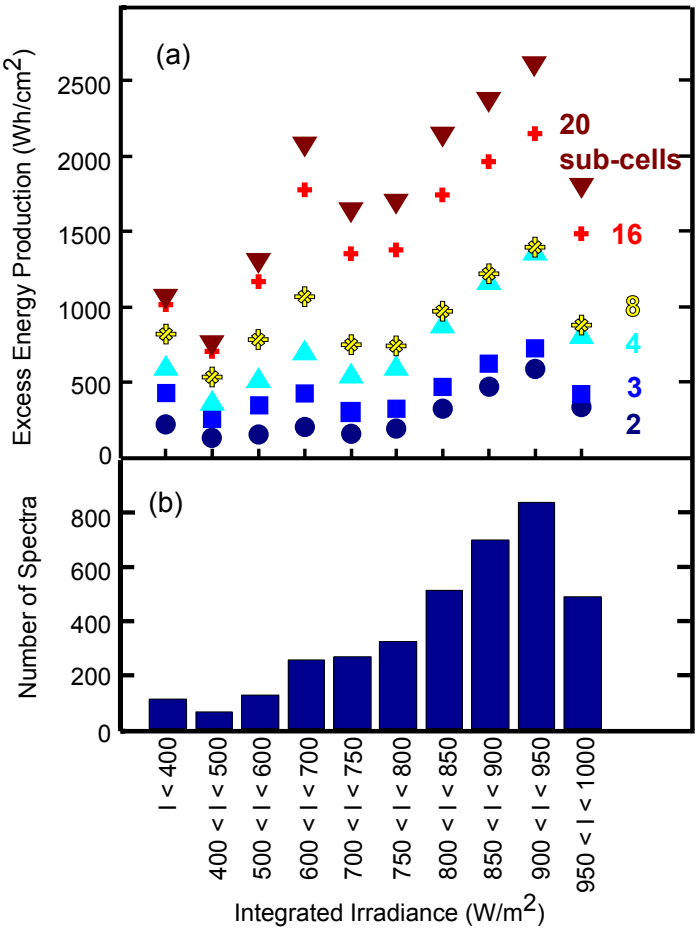

Figure 5.5. Panel (a) shows cumulative additional energy produced by independent ensembles relative to series ensembles over the year's worth of simulated spectra. Panel (b) shows the number of simulated spectra falling in each power level range.

an advantage in capacity factor for the electrically-independent ensembles.

While Figure 5.4 illustrates that series connected ensembles have a significant performance loss under lower incident power, Figure 5.6 compares the performance of series-connected and electrically independent ensembles over the course of the year. Panel a shows the average series-connected efficiency as a percentage of the average electrically independent ensemble efficiency for each month of the year while panel b shows the mean, minimum and maximum incident power for each month. Under AM1.5D the efficiency of a series ensemble as a percentage of the efficiency of the independent ensemble with the same number of cells ranges from 98% for the 2 cell

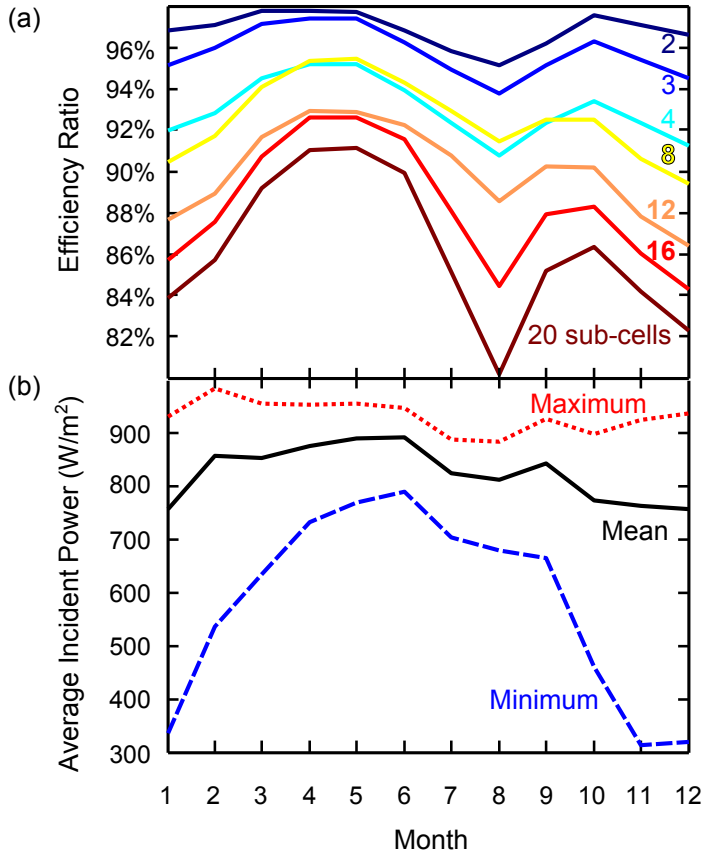

Figure 5.6. Panel (a) shows the monthly power-weighted average efficiency of series-connected ensembles relative to independent ensembles with the same number of sub-cells. Panel (b) shows the monthly minimum, mean and maximum incident power levels.

ensemble to 95% for the 20 cell ensemble. All the relative efficiencies in Figure 3 are lower than the design values. As expected from the efficiency behavior shown in Figure 5.4, the 2 and 3 cell series ensembles have the best performance relative to their independent counterparts. For all ensembles the relative performance is low in the winter months, which have low minimum irradiance levels, comparatively low mean irradiance levels and produce the majority of the low power spectra. Relative performance improves as mean and minimum irradiance increase in spring and early summer and peak in May, before the highest mean irradiance levels. Interestingly, however, the lowest relative performance corresponds to the months of July, August and September, despite the high mean and minimum irradiance levels in those months.

The slight decrease in irradiance in the months of July and August corresponds

to the typical peak of the Arizona monsoon season, which brings increased water vapor in the air column and also increased aerosol optical depth. The absorption and scattering caused by aerosols and water slightly decrease the direct transmission and change the spectral composition, which in turn degrades the series ensemble performance relative to the independent ensembles. Despite irradiance levels that are very close to the AM1.5D level, the performance of the series ensembles is much lower than expected from their design efficiency. It is particularly unfortunate that the series ensemble performance degrades in the peak of summer, when daytime electricity demand is highest in the Phoenix, Arizona area.

5.5 Conclusion

The analysis for Phoenix shows that a photovoltaic system's performance under the standard AM1.5D spectrum may not be a good prediction of its energy production potential under the varying spectral conditions in deployment. Models for projecting energy production that do not account for spectral variation are likely to severely underestimate the advantage of more complex electrical designs.

Choosing the appropriate design for a photovoltaic system at a particular location would benefit from a more detailed energy production prediction like the one described in this chapter. Future work should focus on developing a test standard that can predict energy production performance based on a manageable number of test spectra and atmospheric data for the installation location.

Chapter 6

Conclusions and future directions

The several threads of this thesis are all focused on the design and fabrication of photovoltaic systems with very high efficiency. This is motivated primarily by the sense that efficiency, if it can be obtained at a reasonable cost of manufacture, is highly valuable for reducing the cost of electricity generated from sunlight. In another sense, the pursuit of high efficiency by its nature requires high performance from every aspect of a system's design, in this case band-gap selection, cell radiative efficiency, and optical and electrical system efficiency. Some performance improvements are easier to obtain than others, but aggressively attempting to minimize all loss mechanisms will often identify techniques that can be broadly applied in cost-effective fashion. In particular, the performance enhancement gained from re-optimizing series-connected ensembles accounting for radiative coupling could be integrated straightforwardly into standard MJSC systems.

The annual energy production modeling of Chapter 5, combined with the radiative coupling analysis, suggests another opportunity for performance enhancement. Series-connected designs have traditionally been thought to require close current matching between sub-cells to maximize performance. As Chapter 5 showed, optimizing designs for a particular spectrum will result in lower performance under realistically variable conditions. As chapter 4 showed with the series-connected triple junction example, radiative coupling can mitigate many of the losses caused by current mismatch between sub-cells, provided the system is not current-limited by its top sub-cell. Thus radiative coupling could potentially improve the over-all performance of a system by stabilizing the system efficiency under irradiance conditions that deviate from the design spectrum. This approach may cost the system in "headline" efficiency but

result in greater energy production over the course of a day and year.

In order to validate photovoltaic system designs for energy production, some measurement of system efficiency under varying spectral conditions is required. Ideally such a measurement could be used in combination with site-specific climate data to predict the energy production performance of a system installed in the field. Such a tool would improve the cost projections used to determine the financial viability of a photovoltaic installation. While Chapter 5 shows that electrically independent systems will perform at a level comparable to their performance under the standard spectrum, all current commercially-available high-efficiency solar cells are series connected. The strong correlation between system efficiency and incident irradiance level shown in Chapter 5 suggests a possible test method. A set of new standard spectra, each at a different irradiance level with a spectral composition representative of that level, could be created. Photovoltaic systems would then be tested under each of these new spectra and a power-weighted average efficiency determined. Some amount of location-specific prediction could be achieved by adjusting the weighting factors in the average to reflect the relative prevalence of each irradiance level at the desired location. Using a simple power weighting scheme would allow predictions using direct and diffuse irradiance measurements which are currently available for a wide range of locations, rather than requiring spectrally-resolved irradiance data.

The virtual substrate project was inspired by the advantage lattice-matched growth has over metamorphic growth in terms of optoelectronic quality. While the introduction and successful commercialization of the dilute nitride material family decreases the motivation to pursue new template lattice constants somewhat, the virtual substrate still has potential as a template for other device applications. The next steps of this project should begin with a thorough analytic or numeric analysis of the dynamics of crack formation and strain relaxation in the film during the etching and transfer process. The system is not trivial, and such an analysis will identify limiting dimensions and strain relaxation mechanisms, and would potentially help design an improved transfer method. Once substrates with larger continuous uncracked area can be consistently produced, a thorough examination of the surface quality and bond

strength evolution under growth conditions will be essential.

The analysis of the system effects in radiative coupling is the least developed and, I think, the most exciting direction of work in this thesis. The results presented here, showing potential efficiency improvements for designing series-connected ensembles to account for radiative coupling are preliminary. Future work should extend this analysis to electrically independent ensembles and to systems with non-ideal behavior accounted for.

Bibliography

[1] Weston A. Hermann. Quantifying global exergy resources. *Energy*, 31:1349–1366, 2006. ISSN 03605442. doi: 10.1016/j.energy.2005.09.006. 1

[2] International Energy Agency. Key World Energy Statistics. Technical report, 2013. 1

[3] Energy Information Administration. Annual energy outlook 2014. Technical report, 2014. 1, 2

[4] Office of Energy Projects. Office of Energy Projects Infrastructure Report. Technical report, 2014. URL http://www.ferc.gov/legal/staff-reports/2013/dec-energy-infrast. 1

[5] Black and Veatch. Cost and performance data for power generation technologies. Technical report, 2012. 1, 3

[6] Martin A. Green. *Third Generation Photovoltaics: Advanced Solar Energy Conversion*. Springer, Berlin Heidelberg New York, 1st edition, 2003. 5, 10, 24, 66

[7] P T Landsberg and V Badescu. Solar energy conversion: list of efficiencies and some theoretical considerations - Part II - Results. *Progress in Quantum Electronics*, 22(4):231–255, 1998. URL <GotoISI>://000078624900002. 5

[8] Jenny Nelson. *The Physics of Solar Cells*, volume 57. 2004. ISBN 1-86094-349-7. doi: 10.1063/1.326636. URL http://www.amazon.co.uk/dp/1860943497$\delimiter"026E30F$nhttp://books.google.co.uk/

books?id=s5NN34HLWO8C$\delimiter"026E30F$nhttp://find.shef.ac.uk/primo_library/libweb/action/dlDisplay.do?vid=SFD_VU2&afterPDS=true&institution=44SFD&docId=44SFD_ALMA_DS21177033470001441. 6, 62

[9] P. Wurfel. The chemical potential of radiation. *Journal of Physics C: Solid State Physics*, 15:3967 – 3985, 2000. doi: 10.1088/0022-3719/15/18/012. 6, 28

[10] W Shockley and H J Queisser. DETAILED BALANCE LIMIT OF EFFICIENCY OF P-N JUNCTION SOLAR CELLS. *Journal of Applied Physics*, 32(3):510–&, 1961. URL <GotoISI>://A19613759B00146. 7

[11] G L Araujo and A Marti. ABSOLUTE LIMITING EFFICIENCIES FOR PHOTOVOLTAIC ENERGY-CONVERSION. *Solar Energy Materials and Solar Cells*, 33(2):213–240, 1994. URL <GotoISI>://A1994PA16500010. 7, 9

[12] Eric Wesoff. Sharp Hits Record 44.4% Efficiency for Triple-Junction Solar Cell : Greentech Media, 2013. URL http://www.greentechmedia.com/articles/read/Sharp-Hits-Record-44.4-Efficiency-For-Triple-Junction-Solar-Cell. 9, 33

[13] A Marti and G L Araujo. Limiting efficiencies for photovoltaic energy conversion in multigap systems. *Solar Energy Materials and Solar Cells*, 43(2):203–222, 1996. URL <GotoISI>://A1996VK31900004. 9, 18, 20

[14] K Tanabe. A Review of Ultrahigh Efficiency III-V Semiconductor Compound Solar Cells: Multijunction Tandem, Lower Dimensional, Photonic Up/Down Conversion and Plasmonic Nanometallic Structures. *Energies*, 2(3):504–530, 2009. doi: 10.3390/en20300504. URL <GotoISI>://000276704700003http://www.mdpi.com/1996-1073/2/3/504/pdf. 10, 14, 20, 33

[15] Gautham Nair, Liang-Yi Chang, Scott M Geyer, and Moungi G Bawendi. Perspective on the prospects of a carrier multiplication nanocrystal solar cell. *Nano letters*, 11(5):2145–51, May 2011. ISSN 1530-6992. doi: 10.1021/nl200798x. URL http://www.ncbi.nlm.nih.gov/pubmed/21500807. 10

[16] I Tobias and A Luque. Ideal efficiency of monolithic, series-connected multijunction solar cells. *Progress in Photovoltaics*, 10(5):323–329, 2002. doi: 10.1002/pip.427. URL <GotoISI>://000177057000004http://onlinelibrary.wiley.com/store/10.1002/pip.427/asset/427_ftp.pdf?v=1&t=gkbkdvem&s=57459f813aeaf9581927678b3b2a4d4d8567f04c. 10, 20

[17] John F. Geisz, Myles A. Steiner, Ivan Garcia, Daniel J. Friedman, and Sarah R. Kurtz. The Role of Optical Emission in High Performance III-V Solar Cells. In *Materials Research Society Spring Meeting*, San Francisco, Ca, 2013. 11

[18] F. Dimroth, C. Baur, A.W. Bett, M. Meusel, and G. Strobl. 3-6 junction photovoltaic cells for space and terrestrial concentrator applications. *Conference Record of the Thirty-first IEEE Photovoltaic Specialists Conference, 2005.*, 2005. ISSN 0160-8371. doi: 10.1109/PVSC.2005.1488185. 11

[19] J. F. Geisz, M. a. Steiner, I. Garcia, S. R. Kurtz, and D. J. Friedman. Enhanced external radiative efficiency for 20.8% efficient single-junction GaInP solar cells. *Applied Physics Letters*, 103(4):041118, 2013. ISSN 00036951. doi: 10.1063/1.4816837. URL http://link.aip.org/link/APPLAB/v103/i4/p041118/s1&Agg=doi. 11, 27

[20] C. N. Eisler, R. A Ze'ev, M. T. Sheldon, X. Zhang, and H. A. Atwater. Multijunction Solar Cell Efficiencies: Effect of Spectral Window, Optical Environment and Radiative Coupling. *Energy and Environmental Science*, in review. 11, 61, 66

[21] Mingguo Liu, Geoffrey S. Kinsey, William Bagienski, Aditya Nayak, and Vahan Garboushian. Indoor and Outdoor Comparison of CPV IIIV Multijunction Solar Cells. *IEEE Journal of Photovoltaics*, 3(2):888–892, April 2013. ISSN 2156-3381. doi: 10.1109/JPHOTOV.2012.2230055. URL http://ieeexplore.ieee.org/lpdocs/epic03/wrapper.htm?arnumber=6381428. 12, 13, 74

[22] Marta Victoria, César Domínguez, Steve Askins, Ignacio Antón, and Gabriel Sala. ASTM G173 standard tables for reference solar spectral irradiances.

Japanese Journal of Applied Physics, AM15D:10ND06, 2012. doi: 10.1143/JJAP.51.10ND06. URL http://jjap.jsap.jp/link?JJAP/51/10ND06/$\delimiter"026E30F$nhttp://jjap.jsap.jp/link?JJAP/51/10ND06/pdf. 12, 74

[23] C A Gueymard, D Myers, and K Emery. P ROPOSED REFERENCE IRRADIANCE SPECTRA FOR SOLAR ENERGY SYSTEMS TESTING. *Solar Energy*, 73(6):443–467, 2002. 12, 74

[24] P Foukal, C Fröhlich, H Spruit, and T M L Wigley. Variations in solar luminosity and their effect on the Earth's climate. *Nature*, 443:161–166, 2006. ISSN 0028-0836. doi: 10.1038/nature05072. 12, 75

[25] Oleg Dubovik and Michael D. King. A flexible inversion algorithm for retrieval of aerosol optical properties from Sun and sky radiance measurements, 2000. ISSN 0148-0227. 12

[26] D R Myers and K E Emery. Terrestrial Solar Spectral Modeling Tools and Applications for Photovoltaic Devices Preprint. In *29th IEEE PV Specialists Conference Conference*, number May, 2002. 12, 75

[27] S Kurtz, D Myers, W E McMahon, J Geisz, and M Steiner. A comparison of theoretical efficiencies of multi-junction concentrator solar cells. *Progress in Photovoltaics*, 16(6):537–546, 2008. doi: 10.1002/pip.830. URL <GotoISI>://000259626600009http://onlinelibrary.wiley.com/store/10.1002/pip.830/asset/830_ftp.pdf?v=1&t=glnz0xzj&s=a7fa0cdf5a38f80989ac8df28148930d53b1a789. 14, 35

[28] J F Geisz, D J Friedman, J S Ward, A Duda, W J Olavarria, T E Moriarty, J T Kiehl, M J Romero, A G Norman, and K M Jones. 40.8% efficient inverted triple-junction solar cell with two independently metamorphic junctions. *Applied Physics Letters*, 93(12), 2008. doi: 12350510.1063/1.2988497. URL <GotoISI>://000259799100098http://apl.aip.org/resource/1/applab/v93/i12/p123505_s1?isAuthorized=no. 14, 38

[29] Junction Solar, Muhammad Jamil, Nikolai N Faleev, Robert L Opila, Ian T Ferguson, Senior Member, and Christiana B Honsberg. Design and Realization of Wide-Band-Gap. *32 IEEE ELECTRON DEVICE LETTERS*, 31(1):32–34, 2010. 15, 24, 33, 38, 39

[30] A G Imenes and D R Mills. Spectral beam splitting technology for increased conversion efficiency in solar concentrating systems: a review. *SOLAR ENERGY MATERIALS AND SOLAR CELLS*, 84(1-4):19–69, October 2004. ISSN 0927-0248. doi: 10.1016/j.solmat.2004.01.038. 18, 20

[31] Albert Polman and Harry a Atwater. Photonic design principles for ultrahigh-efficiency photovoltaics. *Nature materials*, 11(3):174–7, March 2012. ISSN 1476-1122. doi: 10.1038/nmat3263. URL http://www.ncbi.nlm.nih.gov/pubmed/22349847. 18

[32] Allen Barnett, Douglas Kirkpatrick, Christiana Honsberg, Duncan Moore, Mark Wanlass, Keith Emery, Richard Schwartz, Dave Carlson, Stuart Bowden, Dan Aiken, Allen Gray, Sarah Kurtz, and Larry Kazmerski. Very High Efficiency Solar Cell Modules. *Progress in Photovoltaics: Research and Applications*, 17 (October 2008):75–83, 2009. doi: 10.1002/pip. 20

[33] C H Henry. LIMITING EFFICIENCIES OF IDEAL SINGLE AND MULTIPLE ENERGY-GAP TERRESTRIAL SOLAR-CELLS. *Journal of Applied Physics*, 51(8):4494–4500, 1980. URL <GotoISI>://A1980KE10700081. 21, 33

[34] A Froitzheim, R Stangl, L Elstner, M Kriegel, and W Fuhs. AFORS-HET: A computer-program for the simulation of heterojunction solar cells to be distributed for public use. *PROCEEDINGS OF 3RD WORLD CONFERENCE ON PHOTOVOLTAIC ENERGY CONVERSION, VOLS A-C*, pages 279–282, 2003. 25, 26

[35] Uwe Rau. Reciprocity relation between photovoltaic quantum efficiency and electroluminescent emission of solar cells. *Physical Review B*, 76(8):1–8, August

2007. ISSN 1098-0121. doi: 10.1103/PhysRevB.76.085303. URL http://link.aps.org/doi/10.1103/PhysRevB.76.085303. 25, 61

[36] Martin a. Green. Radiative efficiency of state-of-the-art photovoltaic cells. *Progress in Photovoltaics: Research and Applications*, 20(4):472–476, June 2012. ISSN 10627995. doi: 10.1002/pip.1147. URL http://doi.wiley.com/10.1002/pip.1147. 25, 27

[37] R K Ahrenkiel, R Ellingson, S Johnston, and M Wanlass. Recombination lifetime of In 0 . 53 Ga 0 . 47 As as a function of doping density. 72(26):3470–3472, 1998. 26

[38] R. K. Ahrenkiel, R. Ellingson, S. Johnston, J. Webb, J. Carapella, and M. Wanlass. Recombination lifetime of In[sub x]Ga[sub 1x]As alloys used in thermophotovoltaic converters. 282(May):282–288, 1999. doi: 10.1063/1.57807. URL http://link.aip.org/link/APCPCS/v460/i1/p282/s1&Agg=doi. 26

[39] B. Sermage, J.L. Benchimol, and G.M. Cohen. Carrier lifetime in p-doped InGaAs and InGaAsP. *Conference Proceedings. 1998 International Conference on Indium Phosphide and Related Materials (Cat. No.98CH36129)*, 2(May):758–760, 1998. doi: 10.1109/ICIPRM.1998.712768. URL http://ieeexplore.ieee.org/lpdocs/epic03/wrapper.htm?arnumber=712768. 26

[40] J.W. Matthews and A.E. Blakeslee. Defects in epitaxial multilayers, 1974. ISSN 00220248. 35, 36

[41] C W Ebert, C L Reynolds Jr, P Wellenius, J G Reynolds, J F Muth, Z Pulwin, D Lee, F Lu, D Dyer, Veeco Corporation, and Elizabeth Ave. OPTIMIZATION OF INGAAS METAMORPHIC BUFFERS FOR TRIPLE JUNCTION SOLAR CELLS. In *Photovoltaic Specialists Conference (PVSC), 2011 37th IEEE*, 2011. 37

[42] P. Chiu, S. Wojtczuk, X. Zhang, C. Harris, D. Pulver, and M. Timmons. 42.3% Efficient InGaP/GaAs/InGaAs concentrators using bifacial epigrowth.

2011 37th IEEE Photovoltaic Specialists Conference, pages 000771–000774, June 2011. doi: 10.1109/PVSC.2011.6186067. URL http://ieeexplore.ieee.org/lpdocs/epic03/wrapper.htm?arnumber=6186067. 38

[43] R R King, D C Law, C M Fetzer, R A Sherif, K M Edmondson, S Kurtz, G S Kinsey, H L Cotal, D D Krut, J H Ermer, and N H Karam. PATHWAYS TO 40 % -EFFICIENT CONCENTRATOR PHOTOVOLTAICS. In *20th European Photovoltaic Solar Energy Conference and Exhibition*, number June, pages 6–10, 2005. 38

[44] Marina S Leite, Emily C Warmann, Gregory M Kimball, Stanley P Burgos, Dennis M Callahan, and Harry a Atwater. Wafer-Scale Strain Engineering of Ultrathin Semiconductor Crystalline Layers. *Advanced materials*, pages 1–7, July 2011. ISSN 1521-4095. doi: 10.1002/adma.201101309. URL http://www.ncbi.nlm.nih.gov/pubmed/21769949. 39

[45] J. W. Hutchinson and Z. Suo. Mixed Mode Cracking in Layered Materials. *Advances in Applied Mechanics*, 29:63–191, 1991. ISSN 00652156. doi: 10.1016/S0065-2156(08)70164-9. 52

[46] B Audoly and A Boudaoud. Buckling of a stiff film bound to a compliant substrate - Part I: Formulation, linear stability of cylindrical patterns, secondary bifurcations. *Journal of the Mechanics and Physics of Solids*, 56(7):2401–2421, 2008. doi: 10.1016/j.jmps.2008.03.003. URL <GotoISI>://000256736000001http://www.sciencedirect.com/science?_ob=MImg&_imagekey=B6TXB-4S08K1K-1-K&_cdi=5586&_user=1010281&_pii=S0022509608000380&_orig=search&_coverDate=07/31/2008&_sk=999439992&view=c&wchp=dGLzVzb-zSkzS&md5=0d0a5d2e9e12c33f3310f2a7b949b0e7&ie=/sdarticle.pdf. 52

[47] Maurizio Dal Colle, Renzo Bertoncellob, and Eugenio Tondellob. Quantitative ARXPS depth profiling characterisation of native oxides grown on In0 . s3 Ga0

. 47As (100) single crystals. *Journal of Electron Spectroscopy and Related Phenomena*, 2048(94), 1994. 53

[48] B Brennan and G Hughes. Identification and thermal stability of the native oxides on InGaAs using synchrotron radiation based photoemission. *Journal of Applied Physics*, 108:22–24, 2010. doi: 10.1063/1.3475499. 53

[49] Myles A Steiner and John F Geisz. Non-linear luminescent coupling in series-connected multijunction solar cells Non-linear luminescent coupling in series-connected multijunction solar cells. *Applied Physics Letters*, 100:251106, 2012. doi: 10.1063/1.4729827. 61

[50] D R Myers and C A Gueymard. Description and Availability of the SMARTS Spectral Model for Photovoltaic Applications. Technical report, 2004. 75

[51] Alexander Sinyuk, Oleg Dubovik, Brent Holben, Tom F. Eck, Francois Marie Breon, John Martonchik, Ralph Kahn, David J. Diner, Eric F. Vermote, Jean Claude Roger, Tatyana Lapyonok, and Ilya Slutsker. Simultaneous retrieval of aerosol and surface properties from a combination of AERONET and satellite data. *Remote Sensing of Environment*, 107:90–108, 2007. ISSN 00344257. doi: 10.1016/j.rse.2006.07.022. 76